

Principles of toroidal geometry optimization for ITG modes (UW-CPTC 14-2)

Mordechai N. Rorvig^{1, a)}

Masters thesis, Dept. of Engineering Physics, University of Wisconsin

(Dated: 27 August 2014)

We employ fluid limit analytic theory of ITG modes and the simplified, local 3-D equilibrium method to further the understanding of optimization for linear ion temperature gradient (ITG) modes in three-dimensional (3-D) configurations. An analytic result shows the instability scales with two principal geometric coefficients, the drift and FLR/polarization coefficient. The analytic results compare well with numerical results over three sequences of selectively chosen 2-D and 3-D geometries. It is shown how the geometries may be analyzed for their ITG instability properties due to their shape, and how the shape controls those properties. The results indicate that there are three most distinctive methods for optimization, via the normal curvature term, integrated local shear-geodesic curvature term, and FLR term. Improvements on the normal curvature are more straightforward, whereas the FLR term depends on improvements to the torsion, local shear, and/or currents (in 2-D). Improvements to the local shear – geodesic curvature term depend on manipulation of the symmetries and polarities of the curvatures. These are elaborated and shown to aid in characterization of the overall surface geometry.

I. INTRODUCTION

It has been strongly argued that the primary design freedom for toroidal confinement systems is the equilibrium shaping^{1,2}. This is particularly true for the three-dimensional (3-D) configurations of stellarators and heliotrons. Theoretical studies have shown how this freedom may be elegantly exploited to reduce neoclassical transport in stellarators³⁻⁵. Initial demonstrations of this neoclassical optimization have been performed⁶, and attention has recently shifted to seek to understand how the configuration may be optimized for turbulent transport⁷⁻¹⁰. The large energy losses due to turbulent transport¹¹ motivate this optimization as a compelling prospect for stellarator design theory.

There are a number of ways in which a designer might seek to optimize the magnetic geometry for turbulent transport. In this paper we attempt to develop the general strategy of turbulence optimization via minimization of linear growth rates for the ion temperature gradient (ITG) mode (see e.g.¹²⁻¹⁴). We restrict our attention to the simplified regime of the low-beta, electrostatic, adiabatic electron ITG mode for simplicity. We also consider only high temperature gradients far from marginality and focus mainly on the *maximum* linear growth rate.

We focus on the linear instability because of its widely accepted driving influence on confinement turbulence, for example, as formalized in plasma quasilinear theory^{15,16}. Furthermore, treatment of linear ITG modes does not necessarily require the inclusion of kinetic effects such as particle trapping or Landau damping, which can complicate the treatment of other modes. The relative simplicity of the linear ITG growth rate, and the simplicity of its relationship to turbulence as compared to other mechanisms such as flow shear¹⁷ or zonal flow¹⁶, make

it a natural starting point for investigation of turbulence optimization. We may note that a few studies of turbulence optimization employing other strategies have been initiated^{18,19}, and some considerations on trapped electron modes (TEM) optimization conditions have been made²⁰.

Investigation of this instability minimization strategy relies on detailed theories of the ITG mode and the magnetic geometry. While these essential theoretical elements have existed for some time, it has not been clear how to translate those elements into a general understanding for an optimization program. One difficulty is that analytic ITG solutions that provide clear understanding can generally only be given for simplistic geometric configurations, too simplistic to provide general guidance. Another difficulty is that to attain a fully realistic geometric treatment, a numerical solution of the global magnetohydrodynamics (MHD) equilibrium equations is required, involving a profuse amount of data for a single equilibrium, let alone a general set of configurations. This combined difficulty has made the potential scope of toroidal shaping optimization a tantalizing yet elusive concept.

We address the instability understanding problem in this paper by employing the numerical gyrokinetics solver GENE²¹ to achieve accurate linear results, and by finding novel eigenfunction averaged solutions to existing analytic ITG mode theories^{22,23}, valid for arbitrarily shaped geometries. We address the equilibrium understanding problem by employing local 3-D magnetostatic equilibrium theory²⁴, which is much simpler and less expensive than global equilibrium theory. While local 3-D equilibrium has been widely used in ideal ballooning studies it has only rarely been applied to microinstability analysis (e.g., reference²⁵).

We emphasize principles of optimization rather than optimization itself because we do not employ any numerical optimization in this study, focusing instead more on the question of what should be optimized, and how. Ef-

^{a)}mrrovig@gmail.com

forts of numerical optimization are being independently pursued and show promising indications^{8–10}. The most practical question from the point of view of the numerical optimization is what should be minimized, i.e. how should an ITG proxy function be defined. Since we pursue the strategy of linear growth rate minimization, the idealized proxy is simply the numerical computation of the growth rate itself.

Thus the present investigation is chiefly concerned with understanding how an accurately computed growth rate depends on the geometry, and how the geometry controls the growth rate. The first of these objectives is specifically pursued by comparison of analytic and numerical growth rate calculations. The analytic model is sufficiently simple to identify which terms most affect the growth rate. The second objective of understanding the potential for geometric control is more difficult, due to the generality of fully 3-D shaping. We approach this task by selectively parametrizing diverse equilibria and identifying their most important characteristics, so as to provide a kind of template for reasoning towards a more general understanding.

The shaping effects in 2-D systems are often characterized by single parameters such as ellipticity, triangularity, and so on. While these may be useful figures of merit for 2-D systems, they are clearly lacking when dealing with as large a number of shaping parameters as exist in 3-D. The relation between the shaping and the instability that we determine here are therefore at a somewhat higher level of abstraction than may be typically understood. One shape parameter correlations such as ellipticity are replaced by the more primitive geometric notions of averaged normal curvature, etc., which are then expected to be determined directly by the numerical optimization code.

The results of the present investigation indicate that the ITG problem reduces primarily to the consideration of only two coefficients, the drift $\hat{\omega}_d$ and FLR/polarization \hat{k}_\perp^2 coefficients, and their six subsidiary components, i.e. the curvatures $\kappa_n, \kappa_g, \tau_n$, the flux surface proximity $|\nabla\psi|$, and the global properties of the net currents σ and rotational transform ι . The local shear often mentioned in the context of shaping effects is linearly related to the torsion and currents, as $s = \sigma + p'\lambda - 2\tau_n$ (see reference²⁴); here we emphasize the torsion τ_n , which is the more primitive geometric quantity and therefore somewhat simpler to comprehend. Note that as we consider the low beta limit, Pfirsch-Schluter currents do not play an important role in our results, though they are well within the scope of the modeling framework.

Next we review the contents of the paper. In section two, we review analytic theory for ITG instability and determine a general analytic solution. In the third section, we review the theory used for modeling of equilibria. In the fourth section, we discuss validation checks employed to determine the consistency of our results with other, more widely tested methods. In the fifth section, we present the results, which include (a) the selection

of configurations of interest, (b) analysis of their geometries, (c) analysis of their instability properties, (d) their eigenmode characteristics, and (e) the development of a more general viewpoint for understanding optimization over general geometries, by reasoning from the prior results.

II. ITG INSTABILITY THEORY AND MODELING

In this section we first review the literature background for ITG instability in general geometry and the effects of shaping on instability. This is followed by the review and comparison of specific analytic models^{22,23} for ITG instability, and the analytic solution procedure used in the present study. We discuss the spectral characteristics of ITG modes, and the possibility of including kinetic effects into the analytic models. The reader interested in skipping to the results need only reference the primary analytic result of equation 14.

A. Overview

The basic physics mechanisms of the ITG instability are discussed in²⁷. Analytic ITG theory typically tries to provide relations for the critical temperature gradient, or relations for the growth rate, depending on system parameters like the safety factor, aspect ratio, and so on. Accurate estimates of the critical gradient threshold are generally thought to require incorporation of kinetic effects (see e.g. reference²²), whereas far from threshold, fluid models are generally expected to suffice (see e.g. reference²⁸). The effects ‘in-surface’ field shaping, i.e. modified shaping of the field within a fixed geometric magnetic surface, due to the magnetic field strength distribution and rotational transform, have been considered in many references. Regarding shear in tokamaks, there is broad consensus that increasingly positive shear is generally good, and negative shear is superior to positive shear, though the specific scalings depend on what instability model is used²⁹.

Any successful description of stellarator shaping effects should generalize to the description of tokamak shaping effects³⁰. Due to spacing constraints we cannot give a detailed summary of all contributions that have been made. References^{28,29,31–45} discuss 2-D flux surface shaping effects on ITG instability.

The effects of 3-D shaping in stellarators have been extensively studied, but the models used have often been simpler than in 2-D studies. The literature can be roughly divided into studies of TEM type modes, which were the first to be studied specifically in stellarators^{20,46–61}, ballooning modes^{62–66}, and ITG modes^{7–9,25,58,67–73}.

B. Review of instability models and definitions

In this paper we focus on two analytic models for the ITG instability, a fluid model^{23,28} and a fluid limit of a kinetic model²². Although we eventually only show results for the kinetic model, which gives more accurate agreement with the GENE results, we begin with discussion of the fluid model. Since the detailed understanding of the geometric coefficients is obviously crucial to the present study, we take care to fully elaborate how they arise from the eikonal formalism and definitions.

We assume electrostatics so that $\tilde{E} = -\nabla\phi$, and adiabatic electrons, so that $\tilde{n}_e/n = e\phi/T_e = \hat{\phi}$, where a tilde denotes a perturbed (linearized) quantity and ϕ is the perturbed electrostatic potential. Here we will always work with hydrogenic ions so $q_i = e, q_e = -e$ where $e = |e|$ is electron charge magnitude. Fluctuations of the form $\hat{\phi} \sim \exp(-i\omega t + i\mathbf{k} \cdot \mathbf{x})$ are assumed, where \mathbf{k} is a generalized wavevector that can be thought of as a vector WKB eikonal or ray¹⁵. The wavevector \mathbf{k} is an object of central importance to be discussed in detail below.

We use the following notation for parallel gradients of a function f , where $\hat{\mathbf{b}} = \mathbf{B}/B$, $\nabla_{\parallel} f = (\hat{\mathbf{b}} \cdot \nabla f)\hat{\mathbf{b}}$, $\nabla_{\parallel}^2 f = \nabla \cdot \nabla_{\parallel} f = \mathbf{B} \cdot \nabla \left(\frac{1}{B^2} \mathbf{B} \cdot \nabla f \right)$, while the perpendicular operators are given as $\nabla_{\perp} f = (\hat{\mathbf{b}} \times \nabla f) \times \hat{\mathbf{b}}$, $\nabla_{\perp}^2 f = \nabla \cdot \nabla_{\perp} f$.

Application of linearized fluid theory in a system with background gradients results in the governing equation for an ITG eigenmode^{23,28},

$$c_s^2 \nabla_{\parallel}^2 \hat{\phi} = -\frac{\omega(\omega - \omega_{*e})}{1 + \frac{1}{\tau} + \frac{1}{\tau} \delta T_i} \hat{\phi} + \omega(\tau \omega_{di} + \omega \rho_s^2 \nabla_{\perp}^2) \hat{\phi}, \quad (1)$$

where the LHS is due to parallel ion dynamics (sound wave), and on the RHS, the first term comes from the adiabatic electron response, the second from a component of the $n_i \mathbf{v}_{E \times B}$ divergence, the third similarly, and the fourth from the polarization drift term ($n_i \mathbf{v}_{pi}$) divergence. Here, $\rho_s^2 = c_s^2/\Omega_i^2$, $c_s^2 = T_e/m_i$, $\Omega_i = eB/m_i$, $\omega_{di} = \mathbf{v}_{di} \cdot \mathbf{k}$, $\mathbf{v}_{di} = \frac{T_i}{eB} \hat{\mathbf{b}} \times (\vec{\kappa} + \frac{\nabla B}{B})$, where $\vec{\kappa} = \hat{\mathbf{b}} \cdot \nabla \hat{\mathbf{b}}$ is the curvature, and $\omega_{*e} = -\frac{T_e}{eB} \hat{\mathbf{b}} \times \nabla \ln n_i \cdot \mathbf{k}$. The ion temperature perturbation is given by

$$\delta T_i = \frac{\omega}{\omega - \frac{5}{3} \mathbf{v}_{di} \cdot \mathbf{k}} \left(\frac{2}{3} - \frac{\omega_{*e}}{\omega} \left(\frac{2}{3} - \eta_i \right) \right). \quad (2)$$

The magnetic field is written in the form $\mathbf{B} = \nabla\psi \times \nabla(\theta - \iota\zeta)^{74}$, where ψ is the toroidal flux, and the straight coordinates θ, ζ and the rotational transform $\iota = \iota(\psi)$ have been introduced. From here on, derivatives with respect to ψ will be denoted with an apostrophe ($'$). Then the eikonal formalism for the mode structure is employed by taking $\hat{\phi}(\mathbf{x}) \sim \hat{\phi}(\eta) e^{ik_{\alpha} S}$, where k_{α} is a dimensionless wavenumber, η is a coordinate along the field line, with $\hat{\phi}(\eta)$ having negligible perpendicular variation, and $S \equiv \theta - \iota(\zeta - \zeta_k)$, where ζ_k is a constant. Then one naturally defines $\mathbf{k} = k_{\alpha} \nabla S$, and, using the definition for S ,

$$k_{\alpha} \nabla S = k_{\alpha} \nabla \alpha + k_{\psi} \nabla \psi, \quad (3)$$

where the constant $k_{\psi} = k_{\alpha} \iota' \zeta_k$ has been defined, and $\alpha = \theta - \iota\zeta$. The defining feature of the formalism is that $\mathbf{B} \cdot \mathbf{k} = 0$, corresponding to the physical picture of modes with long wavelengths along the field line, and short wavelengths in the perpendicular directions. Thus the notations $\mathbf{k} = \mathbf{k}_{\perp}$ are appropriate. These relations for \mathbf{k} are often referred to as the ballooning formalism for toroidal, field-aligned plasma modes⁷⁵⁻⁸⁰.

Using the given definitions, we have the algebraic relation $\mathbf{B} = \nabla\psi \times \nabla S$ and $B^2 = g^{\psi\psi} g^{SS} - (g^{\psi S})^2$. Using these definitions we may then write $\nabla_{\perp} \hat{\phi} = i\mathbf{k}_{\perp} \hat{\phi}$ and $\nabla_{\perp}^2 \hat{\phi} \approx -k_{\perp}^2 \hat{\phi}$, where an $i\nabla \cdot \mathbf{k}_{\perp} \hat{\phi}$ term has been neglected.

The eikonal form for $\hat{\phi}$ is closely related to a coordinate transformation into field aligned coordinates^{81,82}, where $(\psi, \theta, \zeta) \rightarrow (\psi, S, \eta)$, with $\eta = \zeta$, and S as previously defined. In these coordinates \mathbf{B} has the clebsch form $\mathbf{B} = \nabla\psi \times \nabla S$ mentioned above. The parallel derivative becomes $\mathbf{B} \cdot \nabla \hat{\phi} = \partial \hat{\phi} / \partial \eta / \sqrt{g}$, where $\sqrt{g} = (\nabla\psi \cdot \nabla\theta \times \nabla\zeta)^{-1}$ is the jacobian, so that η takes the interpretation of a coordinate that follows along an individual field line. With the use of the field aligned coordinates and the eikonal formalism, equation 2 is reduced from a PDE to ODE problem, with the domain following the path of an individual field line.

Applying the coordinate transformation to the parallel derivative yields the linear operator, k_{\parallel}^2 , where $\nabla_{\parallel}^2 \hat{\phi} = -k_{\parallel}^2 \hat{\phi}$ and the operator is given by

$$k_{\parallel}^2 \hat{\phi} = -\frac{1}{\sqrt{g}^2 B^2} \left[\frac{\partial^2 \hat{\phi}}{\partial \eta^2} - \left(\frac{1}{\sqrt{g}} \frac{\partial \sqrt{g}}{\partial \eta} + \frac{2}{B} \frac{\partial B}{\partial \eta} \right) \frac{\partial \hat{\phi}}{\partial \eta} \right] \quad (4)$$

Under small aspect ratio ordering for a circular torus, the final terms that go like the first derivative can be shown to vanish exactly to first order. This suggests the operator is typically dominated by the second-derivative term. In this paper we always neglect the contribution from the first derivative term in the analytic modeling.

We next introduce a normalized frequency $\hat{\omega} = \rho\omega/c_s$, where ρ is a reference length scale, and a reference magnetic field strength B_0 so that we can write a thermal gyroradius parameter $\rho_{th} = c_s/\hat{\Omega}_i$, where $\hat{\Omega}_i = eB_0/m_i$. Introducing a definition for the density gradient scale length, L_n , we have $L_n^{-1} = -\frac{B_0 \rho_0}{n} \frac{dn}{d\psi}$ and similarly

$$\omega_{*e} = -k_{\alpha} \frac{T_e}{e} \frac{n'_i}{n_i} = \frac{k_{\alpha}}{\rho L_n} \frac{c_s^2}{\hat{\Omega}_i} = \frac{k_{\alpha} \rho_{th}}{\rho L_n} c_s.$$

Then, we introduce reference length scale parameters L_{\parallel}, L_k, L_d , so we can write normalized geometric factors as

$$\hat{B} = B/B_0 \quad (5)$$

$$\hat{k}_{\parallel}^2 = L_{\parallel}^2 k_{\parallel}^2 \quad (6)$$

$$\hat{\omega}_d = L_d^2 \omega_{di} / k_{\alpha} \hat{B} \quad (7)$$

$$\hat{k}_{\perp}^2 = L_k^2 k_{\perp}^2 / k_{\alpha}^2 \hat{B}^2. \quad (8)$$

The k_{α} coefficients are divided out as a notational choice, since k_{α} is a dimensionless constant and we do not wish

it to influence the magnitude of the normalized geometric factors.

Defining a coefficient A and a coefficient W which represents the strength of the temperature gradient drive, $A = 1 + \frac{5}{3\tau}$, $W = \frac{1}{\tau}(\eta_i - \frac{2}{3}) - \frac{5}{3}(1 + \frac{1}{\tau})\frac{\rho}{L_d}\frac{L_n}{L_d}\frac{\hat{\omega}_d}{B}$, and using all the formalism just described, we can write equation 1 in the form of a cubic polynomial in $\hat{\omega}$,

$$\begin{aligned} & \hat{\omega}^3(1 + A\frac{k_\alpha^2\rho_{th}^2}{L_k^2}\hat{k}_\perp^2)\hat{\phi} - \hat{\omega}^2\frac{k_\alpha\rho_{th}}{L_n}(1 + (\frac{5}{3} + A\tau)\frac{L_n}{L_d}\frac{\rho}{L_d}\hat{\omega}_d \\ & - W\frac{k_\alpha^2\rho_{th}^2}{L_k^2}\hat{k}_\perp^2)\hat{\phi} + \hat{\omega}((\frac{5}{3} - W\tau)\frac{k_\alpha^2\rho_{th}^2}{L_d^2}\frac{\rho}{L_n}\hat{\omega}_d - A\frac{\rho^2}{L_\parallel^2}\hat{k}_\parallel^2)\hat{\phi} \\ & - W\frac{k_\alpha\rho_{th}}{L_n}\frac{\rho^2}{L_\parallel^2}\hat{k}_\parallel^2\hat{\phi} = 0. \end{aligned} \quad (9)$$

We will also be interested in a simplification of 9 where the temperature resonance in 2 is neglected under the standard assumption $\hat{\omega}_d/\hat{\omega} \ll 1$. While the validity of this approximation may be called into question, we find (for the specific parameter regimes of our results) that inclusion of the term makes little difference. It also allows for useful simplification of the equation. We also take $W = \frac{1}{\tau}(\eta_i - \frac{2}{3})$, a very good approximation as long as $\eta_i \gg 1$. These two approximations together give the simplified form of 9,

$$\begin{aligned} & \hat{\omega}^3(1 + A\frac{b}{L_k^2}\hat{k}_\perp^2)\hat{\phi} - \hat{\omega}^2\frac{\sqrt{b}}{L_n}(1 + A\tau\frac{L_n}{L_d}\frac{\rho}{L_d}\hat{\omega}_d - W\frac{b}{L_k^2}\hat{k}_\perp^2)\hat{\phi} \\ & + \hat{\omega}(-W\tau\frac{b}{L_d^2}\frac{\rho}{L_n}\hat{\omega}_d - A\frac{\rho^2}{L_\parallel^2}\hat{k}_\parallel^2)\hat{\phi} - W\frac{\sqrt{b}}{L_n}\frac{\rho^2}{L_\parallel^2}\hat{k}_\parallel^2\hat{\phi} = 0, \end{aligned} \quad (10)$$

where $b = (k_\alpha\rho_{th})^2$.

Writing the ITG equation in the polynomial form in $\hat{\omega}$ has several useful advantages. Firstly, it allows a clear inspection of traditional ITG mode limits. The first of these is the slab limit, given by balancing the adiabatic electron response (the cubic order term in ω) with the parallel dynamics term (zeroth order in ω). This is the standard ‘‘negative compressibility’’ ITG solution. The second limit is the balance of the electron response with the toroidal curvature term that is first order in ω , which gives the standard curvature driven mode.

We next introduce the results of an analytic gyrokinetic model, following the treatment given in²². Using the fluid limit of the model and the notations introduced above, we arrive at the governing eigenmode equation (equation 11 in²²),

$$\begin{aligned} & \hat{\omega}^3(1 + \frac{b}{L_k^2}\hat{k}_\perp^2)\hat{\phi} - \hat{\omega}^2\frac{\sqrt{b}}{L_n}(1 + 2\frac{L_n}{L_d}\frac{\rho}{L_d}\hat{\omega}_d \\ & - W_K\frac{b}{L_k^2}\hat{k}_\perp^2)\hat{\phi} + \hat{\omega}(-2W_K\frac{b}{L_d^2}\frac{\rho}{L_n}\hat{\omega}_d - \frac{1}{2}\frac{\rho^2}{L_\parallel^2}\hat{k}_\parallel^2)\hat{\phi} \\ & - W_K\frac{\sqrt{b}}{L_n}\frac{1}{2}\frac{\rho^2}{L_\parallel^2}\hat{k}_\parallel^2\hat{\phi} = 0, \end{aligned} \quad (11)$$

where here the drive coefficient is modified as $W_K = \frac{1}{\tau}(1 + \eta_i)$.

We will also be interested in a limit of 11 where we neglect the slab destabilization term (zeroth order in $\hat{\omega}$), written here below for completeness,

$$\begin{aligned} & \hat{\omega}^2(1 + \frac{b}{L_k^2}\hat{k}_\perp^2)\hat{\phi} - \hat{\omega}^1\frac{\sqrt{b}}{L_n}(1 + 2\frac{L_n}{L_d}\frac{\rho}{L_d}\hat{\omega}_d - W_K\frac{b}{L_k^2}\hat{k}_\perp^2)\hat{\phi} \\ & + (-2W_K\frac{b}{L_d^2}\frac{\rho}{L_n}\hat{\omega}_d - \frac{1}{2}\frac{\rho^2}{L_\parallel^2}\hat{k}_\parallel^2)\hat{\phi} = 0. \end{aligned} \quad (12)$$

Except for the differences in prefactors, equations 10 and 11 have an identical structure. Note however that in the kinetic model, no assumption was made on η_i , b was assumed small, and the \hat{k}_\perp^2 term arises from the effect of averaging over the gyroradius (the Bessel function) – the so-called finite larmor radius (FLR) effects. Also, in the fluid model, no assumption was made on the relative magnitudes of ω/k_\parallel and v_{th} (until going from equation 9 to 10). The structural agreement in the models gives confidence in the cubic (or quadratic) nature of the ITG mode dispersion problem.

C. Generalized analytic solution and implications

The ODE eigenvalue problem is Schrodinger type, but general solutions are difficult due to the complex dependence of the generalized potential on the eigenfrequency. The solution approach employed here makes use of the fact that the eigenmodes should be localized, a feature not necessarily true for all modes (e.g., ideal MHD interchange modes⁷⁸) but which should be true for drift modes. Therefore, we can define an average, which applied to a function f goes like

$$\langle f \rangle = \int_a^b d\eta \hat{\phi}^* f \hat{\phi} / \int \int_a^b d\eta |\hat{\phi}|^2. \quad (13)$$

Of course, for the method to be sensible, the eigenfunction must be localized within the (a, b) range or periodic about it. Applying this average gives a characteristic polynomial for $\hat{\omega}$ which can then be determined analytically by guessing a form for the eigenfunction $\hat{\phi}$.

The idea is that the eigenfunction can be approximated as a gaussian centered around the point of worst curvature. This is motivated by the recurring appearance of gaussian type eigenmodes in numerical microinstability studies. In this work the imaginary part of the eigenfunction is always assumed to be constant and neglected. This eigenfunction modeling approach is somewhat similar to a method used by Puztai et. al.⁸³, which assumes a generic form for the eigenfunction and then fits the coefficients using a similar principle of integrability. The authors know of at least one other case in the literature⁸⁴ where such an approach of guessing the eigenfunction has been used.

More specifically, we assume that the mode width is determined such that the squared eigenfunction is contained within one poloidal transit along the field line. So,

for example, for a mode centered at the outboard mid-plane, with mode width σ_1 so that for $\hat{\phi} \sim \exp(-\eta^2/2\sigma_1^2)$, $\hat{\phi}^2 \sim \exp(-\eta^2/\sigma_1^2) = \exp(-\eta^2/2\sigma_2^2)$, where $\sigma_2 = \sigma_1/\sqrt{2}$,

the full width quantity ($\sim 6\sigma_2$) is set equal to the $2\pi/\iota$ (for $\theta = \iota\eta$ on a given field line).

Applying the average here to equation 12 gives a closed form, quadratic solution for $\hat{\omega}$ and $\gamma = \text{Im}\{\hat{\omega}\}$,

$$\gamma(b) = \pm \frac{\sqrt{\frac{\sqrt{b}}{L_n}(-1 - 2\frac{\rho L_n}{L_d^2}\langle\hat{\omega}_d\rangle + W_K\frac{b}{L_k^2}\langle\hat{k}_\perp^2\rangle)^2 + 4(1 + \frac{b}{L_k^2}\langle\hat{k}_\perp^2\rangle) \cdot (2W_K\frac{b\rho}{L_d^2 L_n}\langle\hat{\omega}_d\rangle + \frac{1}{2}\frac{\rho^2}{L_\parallel^2}\langle\hat{k}_\parallel^2\rangle)}}{2(1 + \frac{b}{L_k^2}\langle\hat{k}_\perp^2\rangle)}. \quad (14)$$

Equation 14 is a simple but important result. It is quite generally applicable since it is independent of the specific guess for the eigenfunction. Since the signs of the terms are now all manifest, in particular $W_K > 0$ and for a gaussian eigenfunction, $k_\parallel^2 \hat{\phi} > 0$, it clearly indicates how $\langle\hat{\omega}_d\rangle < 0$ is a necessary condition for instability – thus rigorously manifesting the phenomena of bad (negative) curvature instability drive. Furthermore, the $\langle\hat{k}_\perp^2\rangle$ term is seen to be uniformly stabilizing, with the growth rate scaling roughly as $\langle\hat{k}_\perp^2\rangle^{-0.5}$. As noted above, the \hat{k}_\perp^2 term arises due to divergence of the ion polarization drift, or the Bessel term due to the finite larmor radius in the gyrokinetic model. For that reason, we refer to it as the FLR, or polarization term.

D. Spectral dependence and kinetic effects

One might expect that an ITG instability optimized geometry should have fundamental alterations to its instability spectra (its variation with b) as compared to an unoptimized geometry. In this study, we emphasize the maximum linear growth rate over the spectra, in order to preserve focus, and considering the most unstable mode as characteristic of the overall instability drive. Despite this simplification, the spectral characteristics are an important feature of the ITG mode.

Although the characteristic spectra are well known, they are not often explained. Since the polarization term scales with b , the ITG mode stabilizes as b increases. However, the curvature drive term $\hat{\omega}_d$ also scales with b , so for small b the curvature drive leads to increasing instability with decreasing b . Curvature drive increasing with decreasing perpendicular wavelength is a feature shared by the basic Rayleigh-Taylor type mode⁸⁵ and hence can be understood as a generic Rayleigh-Taylor type effect. These two features together describe a canonical spectrum for toroidal ITG mode instability, which looks roughly like an inverted parabola centered in the x -axis around $k_\alpha \rho_{th} \sim 0.3$, with the width of the parabola roughly determined such that $\gamma < 0$ at $k_\alpha \rho_{th} = 0$. Polarization optimization via maximization of \hat{k}_\perp^2 should bias and shift the spectrum to center at lower $k_\alpha \rho_{th}$, which is what is observed in the numerical results in section four.

It would be of interest to consider elementary kinetic effects on the eigenmode, but such extensions greatly increase the complexity of the analytic models. They also lend fundamental complications to the spectral behaviour of the analytic results. Romanelli considers a local kinetic limit (equation 19 and 20 in²²) which is the most straightforward way to incorporate kinetic effects into the analytic model. However, he does not include the J_0^2 correction, which we find to be crucial via the result of 14. Including this term, and then repeating the calculation by adopting the “grad-B model”⁸⁶ $\mathbf{v}_d = \frac{1}{\Omega_i} \hat{\mathbf{b}} \times (\nabla \ln B + \kappa)(v_\perp^2)$, and expanding the Bessel function as before, we find the dispersion relation

$$\begin{aligned} \left(1 + \frac{1}{\tau}\right) &= e^z \left(z \left(1 - \eta_i \frac{\omega_*}{\bar{\omega}_d}\right) + \frac{\omega_*}{\bar{\omega}_d} (1 - \eta_i) \right) \\ &\times E_1(z) \left(1 + \frac{1}{2} \frac{k_\perp^2 v_{th}^2}{\Omega_i^2} z\right) + \frac{\omega_*}{\bar{\omega}_d} \eta_i \\ &+ \frac{1}{2} \frac{k_\perp^2 v_{th}^2}{\Omega_i^2} \left(-z - \frac{\omega_*}{\bar{\omega}_d} (1 - z)\right), \end{aligned} \quad (15)$$

where $z = -\omega/\bar{\omega}_d$ and E_1 is an exponential integral, $E_1(z) = \int_z^\infty dz e^{-z}/z$. Asymptotically, for $z \gg 1$ and $\text{Re}\{z\} < 0$, one can write $E_1(z) \approx e^{-z}/z(1 - 1/z + 2/z^2 - \dots) - i\pi$, giving the Landau-like damping effect from resolving the contribution of a pole in velocity space.

Equation 15 is of considerable interest, but it is also much more complicated than the model equations 10 and 12. First of all, the most tractable expansion limit $z \gg 1$ is opposite to the traditional fluid limit of the other models. Another complication is that the curvature terms, FLR terms, and damping terms are multiplicatively coupled. This coupling means that \hat{k}_\perp^2 effects will no longer be uniformly stabilizing. This explains why fully kinetic ITG calculations may demonstrate spectra with a “tail” of instability at higher $k_\alpha \rho_{th}$ than the standard inverse parabolic type spectra discussed above. To avoid these complications, we do not pursue any further detailed analytic modeling or solution of the kinetic ITG effects. We also work in gradient regimes expected to be far from marginal levels, $\eta_i = 10$, so that kinetic threshold effects are not expected to be significant.

E. Summary

In summary, we have derived several expressions for the ITG mode dependency on geometric coefficients. The key geometric quantities are the polarization or FLR coefficient, $\langle \hat{k}_\perp^2 \rangle$, and the curvature drift coefficient $\langle \hat{\omega}_d \rangle$. The basic objective for the geometry has been made clear, i.e., to maximize $\langle \hat{k}_\perp^2 \rangle$ without concern for sign, and to make the curvature term $\langle \hat{\omega}_d \rangle$ as positive (or least negative) as possible. For the purposes of the analytic model results, presented below, the eigenfunction is assumed to have a gaussian mode structure.

III. MAGNETIC GEOMETRY THEORY AND MODELING

In this section we review the modeling of the toroidal magnetic geometry. Firstly we introduce the local 3-D equilibrium analytic formalism²⁴ for modeling of a single equilibrium magnetic surface. Next we describe the formal relations between the geometry and the growth rate solution presented above. Lastly we clarify some subtleties involved in the technical step of specifying the straight field line coordinate mappings.

A. Local 3-D equilibrium theory

In this work we apply the analytic theory of local 3-D equilibrium for modeling and understanding of the magnetic structure. The theory consists chiefly in the formal relations and constraints which describe and relate the geometric properties of a magnetic surface. It is simple enough that it can be relatively rapidly implemented by computer, furnishing all the necessary geometric data for solution of the instability models.

The local 3-D theory arose out of efforts to develop simplified equilibrium models for flux surface shaping effects in tokamaks, as in⁴² and references therein. In particular, these models were motivated by the fact that the eikonal formalism instability calculations (as presented in section two) only require geometric information for a single magnetic surface. While global equilibrium solutions provide this data for all the surfaces within an equilibrium, they are both more expensive and difficult to analyze, given the profuse amount of data involved. It should also be emphasized that the general relations of local 3-D theory are *exact* in the context of magnetostatic MHD equilibrium and therefore very generally useful for understanding. Every global solution must satisfy the local theory on every magnetic surface; the converse does not hold.

After the initial 3-D magnetostatic formulation²⁴, Boozer recognized its utility⁸⁷ and Skovoroda realized its place within classical differential geometry⁸⁸⁻⁹⁰, among other intriguing relations. Unlike the 2-D local theory, the local 3-D equilibrium theory has only rarely been ap-

plied to instability analysis (see e.g. references^{25,62,64}), so we provide a careful review of the theory here.

The basic idea of the theory is the following. In order to model the effects of toroidal field shaping on microinstability, we must be able to write down the expressions for the magnetic field on an arbitrarily shaped toroidal surface. For example, any parametrization of a surface $\mathbf{x}(u_1, u_2)$ immediately furnishes coordinate curves $\mathbf{x}_{u_1} = \partial \mathbf{x} / \partial u_1$, $\mathbf{x}_{u_2} = \partial \mathbf{x} / \partial u_2$ which could then be used as the linearly independent basis vectors for a field \mathbf{B} on the surface. Once the field and the surface are chosen, the currents may be calculated via Ampere's law $\nabla \times \mathbf{B} = \mu_0 \mathbf{J}$ and we could then in principle perform any desired equilibrium dependent calculation.

Crucially however, the magnetic field cannot be an arbitrary toroidal vector field – it must be consistent with the MHD equilibrium equations. Local equilibrium theory satisfies exactly this requirement, i.e., it consists in the set of relations for the most general toroidal surface field consistent with the equilibrium equations.

A vital reason why the local theory works is because of the appropriate application of coordinates, which eliminates the need to provide a radial parametrization of the equilibrium, the constraints for which are significantly more complicated than the constraints on a single surface. For this reason we discuss the coordinate parametrizations in much greater detail than the original reference²⁴, which included only selective calculations.

B. Analytic formalism

Next we give the analytic formalism, reviewing the results of²⁴. The basic procedure may be described as follows, making reference to the formulas below.

Specifying the surface shape $\mathbf{x}(\psi_0, \theta, \zeta)$, the straight field line coordinates $\theta(\mathbf{r})$ and $\zeta(\mathbf{r})$ to be defined below, and the transform ι , the magnetic field is calculated via 27. The curvatures may then be calculated directly, as will be shown below. The self-consistent MHD jacobian solution (if one exists) is determined via 28; this is the primary constraint on choosing the shaping and equilibrium parameters. Next, two of the three quantities p', ι', σ are specified, and the third solved via 38. The integrated local shear of equation 33, crucial for the instability analysis, is then determined up to a constant. The magnetic surface properties are then completely specified. In what follows, we elaborate this process in detail.

Assume that we have a closed magnetic flux surface labeled by the toroidal flux, ψ , so that $\nabla \psi = dp/d\psi \nabla \psi$. Define the unit tangent vector $\hat{\mathbf{b}} = \mathbf{B}/B$ and unit normal $\hat{\mathbf{n}} = \nabla \psi / |\nabla \psi|$. With curvature $\kappa = \hat{\mathbf{b}} \cdot \nabla \hat{\mathbf{b}}$, then MHD equilibrium $\mathbf{J} \times \mathbf{B} = \nabla p$ implies $\mathbf{B} \cdot \nabla \mathbf{B} = \nabla(\mu_0 p + \frac{B^2}{2}) = B^2 \kappa + B(\hat{\mathbf{b}} \cdot \nabla B) \hat{\mathbf{b}}$ which can be rewritten as

$$\nabla B = B\kappa + (\hat{\mathbf{b}} \cdot \nabla B) \hat{\mathbf{b}} - \mu_0 p' \frac{|\nabla \psi|}{B} \hat{\mathbf{n}}. \quad (16)$$

Since pressure gradients are often small compared to the magnetic field, the gradient of the field strength is often dominated by the field curvature.

The field curvatures as well as the curvatures of the normal and binormal fields may be introduced as

$$(\hat{\mathbf{b}} \cdot \nabla) \hat{\mathbf{b}} = \kappa_n \hat{\mathbf{n}} + \kappa_g \hat{\mathbf{b}} \times \hat{\mathbf{n}} \quad (17)$$

$$(\hat{\mathbf{b}} \cdot \nabla) \hat{\mathbf{n}} = -\kappa_n \hat{\mathbf{b}} + \tau_n \hat{\mathbf{b}} \times \hat{\mathbf{n}} \quad (18)$$

$$(\hat{\mathbf{b}} \cdot \nabla) \hat{\mathbf{b}} \times \hat{\mathbf{n}} = -\tau_n \hat{\mathbf{n}} - \kappa_g \hat{\mathbf{b}}. \quad (19)$$

where these formulas implicitly define the curvature components, e.g., $\kappa_n \equiv \hat{\mathbf{n}} \cdot (\hat{\mathbf{b}} \cdot \nabla) \hat{\mathbf{b}}$, etc. The three unit vector fields define an orthonormal *frame field* on the surface, with the normal curvature κ_n , geodesic curvature κ_g , and normal torsion τ_n being the *connection forms* of the magnetic vector field, a generalization of the Frenet formulas for a curve^{91,92}. On a cylinder, torsion is just the measure of twisting of a field line around the central axis, and normal curvature the measure of radial curvature, whereas geodesic curvature is zero for a helical curve on a cylinder, becoming nonzero when the cylinder is wrapped into a torus. The normal curvature negativity (positivity) manifests the convexity (concavity) of the surface with respect to the direction of the field. Positivity (negativity) in the torsion manifests the clockwise (counterclockwise) rotation of the normal with respect to the surface.

The magnetic surface current properties are constrained by the MHD equations. The MHD quasineutrality condition $\nabla \cdot \mathbf{J} = 0$ is given by

$$\mathbf{B} \cdot \nabla (\mathbf{J} \cdot \mathbf{B} / B^2) + \nabla \cdot (\mathbf{B} \times \nabla p / B^2) = 0, \quad (20)$$

with homogeneous and inhomogeneous solution

$$\mu_0 \frac{\mathbf{J} \cdot \mathbf{B}}{B^2} = \sigma + p' \lambda, \quad (21)$$

where $\sigma = \mu_0 \langle \mathbf{J} \cdot \mathbf{B} \rangle / \langle B^2 \rangle$ is the flux surfaced average current, with the property of the flux surface average being $\mathbf{B} \cdot \nabla \sigma = 0$ ⁷⁴.

For arbitrary surface coordinates θ, ζ defined so that $\mathbf{x}(\theta, \zeta)$ is periodic in $[0, 2\pi]$, the flux surface average – not to be confused with the eigenfunction average defined above – of an arbitrary function $f(\psi, \theta, \zeta)$ may be defined as

$$\langle f \rangle = \frac{\oint d\theta \oint d\zeta \sqrt{g} f}{V'}, \quad (22)$$

where $\sqrt{g} = (\nabla \psi \cdot \nabla \theta \times \nabla \zeta)^{-1}$ and $V' = dV/d\psi = \oint d\theta \oint d\zeta \sqrt{g} / (2\pi)^2 = (\sqrt{g})_{00}$, the zero-zero fourier harmonic in an expansion for the jacobian, i.e., $\sqrt{g} = V'(1 + \sum_{(m,n) \neq (0,0)} (\sqrt{g})_{mn} e^{i(m\theta + n\zeta)})$. The value of V' serves as an overall normalization factor that can be dimensionally estimated as $V' \approx R_0/B_0$, assuming $V \approx R_0 \rho^2$ (where R_0 is a toroidal major radius and ρ a minor radius) and $\psi \approx B_0 \rho^2$.

The quantity $p' \lambda$ is called the Pfirsch-Schluter current and λ the Pfirsch-Schluter coefficient. The coefficient λ is

determined from 20 and 21 by applying $\mathbf{B} \cdot \nabla$ and making use of 16 and 17 to get

$$\mathbf{B} \cdot \nabla \lambda = 2\mu_0 \frac{|\nabla \psi|}{B} \kappa_g. \quad (23)$$

We may also introduce the local shear, defined as

$$s = \hat{\mathbf{b}} \times \hat{\mathbf{n}} \cdot \nabla \times (\hat{\mathbf{b}} \times \hat{\mathbf{n}}). \quad (24)$$

The local shear is directly related to the current properties of the equilibrium and its torsional curvature properties. The currents may be written $\mu_0 \frac{\mathbf{J} \cdot \mathbf{B}}{B^2} = \hat{\mathbf{b}} \cdot \nabla \times \hat{\mathbf{b}}$, so that a purely algebraic or geometric relation may derived,

$$s = \sigma + p' \lambda - 2\tau_n. \quad (25)$$

Up to now we have said nothing about the functional form of the surface coordinates ψ, θ, ζ other than that they are straight field line coordinates, meaning they define the field via the expression

$$\mathbf{B} = \nabla \psi \times \nabla (\theta - \iota \zeta). \quad (26)$$

Straight coordinates have been well reviewed^{1,74,87,93,94}, but can be somewhat obscured because the analytic mappings between straight coordinates and geometric coordinates (cylindrical, toroidal, etc.) are rarely derived. One example is⁴⁷ where the mapping between a straight, helical stellarator and Boozer coordinates, a particular choice of straight field line coordinates, is given. One of the difficulties in determining the mapping is that the relation between the geometric radial coordinate and the straight flux surface labeling coordinate is generally intractable, even for simple, straight stellarators⁹⁵. Another difficulty is the determination of the surface transform ι , tractable only at fixed radial distance values and therefore valid only for very weak surface shaping³⁰. We will discuss how to parametrize these coordinates below.

The magnetic field expression 26 is formally equivalent to

$$\mathbf{B} = \frac{1}{\sqrt{g}} \left(\frac{\partial \mathbf{x}}{\partial \zeta} + \iota \frac{\partial \mathbf{x}}{\partial \theta} \right), \quad (27)$$

which is shown using the elementary theory of reciprocal basis vectors or general coordinates^{1,74}, crucial for the local 3-D equilibrium theory.

The function $\iota = \iota(\psi)$ is the rotational transform, representing the average number of poloidal circuits a field line makes for every toroidal circuit. The coordinates θ, ζ are called straight because 26 implies $\iota = \frac{\mathbf{B} \cdot \nabla \theta}{\mathbf{B} \cdot \nabla \zeta}$. In local equilibrium, it is not possible to self-consistently calculate the transform for a given surface shape, since the transform depends on the external coil configuration which is unspecified. Thus ι is treated as an input parameter. However, there is a strong correlation between the extent of surface *turning* and the magnitude of ι (as discussed e.g. in reference³⁰), such that solution of equation 28 depends on judicious choice of ι for any given shape. The transform is thus functionally associated with the number and extent of the field periods of the device (see

e.g. reference⁹⁶), as it would be for any global equilibrium solution method, despite being treated as a free parameter in the local theory.

The MHD currents must lie within the surface. The condition $\mathbf{J} \cdot \hat{\mathbf{n}} = 0$ is then given by

$$\frac{\partial}{\partial \theta} \frac{g_{\zeta\zeta} + \iota g_{\zeta\theta}}{\sqrt{g}} = \frac{\partial}{\partial \zeta} \frac{g_{\theta\zeta} + \iota g_{\theta\theta}}{\sqrt{g}}. \quad (28)$$

With the surface parametrization $\mathbf{x}(\theta, \zeta)$, ι , and the coordinate transformations (e.g. $\theta(\mathbf{r})$, where \mathbf{r} is a position vector) specified, this equation is viewed as a constraint on the Jacobian. The remarkable feature of the constraint is that it does not depend on the global, radial parametrization of the equilibrium.

The constraint 28 is quite general and must also be satisfied for a vacuum surface. To see that, note in general coordinates the curl of a vector field may be written $\nabla \times \mathbf{B} = \sum_k (\partial B_j / \partial u^i - \partial B_i / \partial u^j) \mathbf{e}_k$, so that in vacuum, each component must separately vanish. The vanishing of the first vector component $k = 1$ is then given by $\partial B_3 / \partial \theta = \partial B_2 / \partial \zeta$, which is identical to 28. In vacuum one can decompose $\mathbf{B} = \nabla V = \partial V / \partial \psi \nabla \psi + \partial V / \partial \theta \nabla \theta + \partial V / \partial \zeta \nabla \zeta$, so trivially $B_2 = \partial V / \partial \theta$ and similarly $B_3 = \partial V / \partial \zeta$, and 28 is identically zero. However, in practice, it is easier to parametrize the surface $\mathbf{x}(\theta, \zeta)$ explicitly than to find appropriate harmonic parametrizations for V , so 28 must still be imposed.

In the case of axisymmetry (taking $\zeta \sim \phi$) the right hand side of equation 28 is trivially zero and the jacobian can be found analytically as $\sqrt{g} = C g_{\zeta\zeta}$, where C is a constant. In the results section of this paper we will generally be using numerical solution for the jacobian making use of standard truncated finite fourier expansions, and similarly for the Pfirsch Schluter coefficient and field line quantities. Failure of an equilibrium shape to satisfy 28 is manifested by increasing divergence or sign change in the magnitude of \sqrt{g} (and hence fundamentally B and $|\nabla \psi|$), as well as striation in its surface distribution, as the extent of the shaping is made increasingly inappropriate.

Once the jacobian is determined, \mathbf{B} and $\nabla \psi$ may be written down. Noting $\partial_\zeta \mathbf{e}_R(\phi) = -\partial_\phi \mathbf{e}_R(\phi) = \sin \phi \hat{\mathbf{x}} - \cos \phi \hat{\mathbf{y}} = -\mathbf{e}_\phi$, the curvatures may be explicitly calculated. Define coefficients related to the length and area elements on the surface, $L = \sqrt{g_{\zeta\zeta} + 2\iota g_{\zeta\theta} + \iota^2 g_{\theta\theta}}$, $A = \sqrt{g_{\theta\theta} g_{\zeta\zeta} - g_{\theta\zeta}^2}$. Then the curvature expressions take the form

$$\begin{aligned} \kappa_n &= \frac{1}{AL^2} \\ &\times [RZ_\theta(R_{\zeta\zeta} - R) + (Z_\theta R_\zeta - R_\theta Z_\zeta)(-2R_\zeta) - RR_\theta Z_{\zeta\zeta} \\ &+ 2\iota(RZ_\theta R_{\theta\zeta} - (Z_\theta R_\zeta - R_\theta Z_\zeta)R_\theta - RR_\theta Z_{\theta\zeta}) \\ &+ \iota^2(RZ_\theta R_{\theta\theta} - RR_\theta Z_{\theta\theta})] \end{aligned}$$

$$\begin{aligned} \kappa_g &= \frac{1}{AL^3} \\ &\times [(g_{\zeta\zeta} + \iota g_{\zeta\theta})R_\theta - (g_{\theta\zeta} + \iota g_{\theta\theta})R_\zeta](R_{\zeta\zeta} - R + 2\iota R_{\theta\zeta} + \iota^2 R_{\theta\theta}) \end{aligned}$$

$$\begin{aligned} &+ (g_{\theta\zeta} + \iota g_{\theta\theta})R(-2R_\zeta - 2\iota R_\theta) \\ &+ ((g_{\zeta\zeta} + \iota g_{\zeta\theta})Z_\theta - (g_{\theta\zeta} + \iota g_{\theta\theta})Z_\zeta)(Z_{\zeta\zeta} + 2\iota Z_{\theta\zeta} + \iota^2 Z_{\theta\theta}) \end{aligned} \quad (30)$$

$$\begin{aligned} \tau_n &= \frac{1}{A^2 L^2} \\ &\times [(g_{\theta\zeta} + \iota g_{\theta\theta})(RZ_\theta(R_{\zeta\zeta} - R + \iota R_{\theta\zeta}) \\ &+ (Z_\theta R_\zeta - R_\theta Z_\zeta)(-2R_\zeta - \iota R_\theta) - RR_\theta(Z_{\zeta\zeta} + \iota Z_{\theta\zeta})) \\ &- (g_{\zeta\zeta} + \iota g_{\zeta\theta})(RZ_\theta(R_{\theta\zeta} + \iota R_{\theta\theta}) \\ &+ (Z_\theta R_\zeta - R_\theta Z_\zeta)(-R_\theta) - RR_\theta(Z_{\theta\zeta} + \iota Z_{\theta\theta}))]. \end{aligned} \quad (31)$$

To relate the surface shear to the local shear, the radial derivative at the surface may be calculated as

$$\frac{\partial \mathbf{x}}{\partial \psi} = \frac{1}{|\nabla \psi|} \hat{\mathbf{n}} + \frac{h}{B} \hat{\mathbf{b}} + D \frac{|\nabla \psi|}{B} \hat{\mathbf{b}} \times \hat{\mathbf{n}}, \quad (32)$$

where the components h, D are calculated via orthonormal expansion, using the relations of general coordinates. For example, we have $\mathbf{x}_\psi \cdot \hat{\mathbf{b}} \times \hat{\mathbf{n}} = \sqrt{g} \nabla \theta \times \nabla \zeta \cdot \frac{\mathbf{B} \times \nabla \psi}{B |\nabla \psi|} = \frac{\sqrt{g}}{B |\nabla \psi|} (g^{\psi\zeta} \mathbf{B} \cdot \nabla \theta - g^{\psi\theta} \mathbf{B} \cdot \nabla \zeta) = \frac{|\nabla \psi|}{B} \frac{\iota g^{\psi\zeta} - g^{\psi\theta}}{g^{\psi\psi}}$, giving the binormal expansion coefficient, $D = \frac{\iota g^{\psi\zeta} - g^{\psi\theta}}{g^{\psi\psi}}$. The $D |\nabla \psi| / B$ term is closely related to the local shear, measuring how much the flux surfaces are binormally displaced. Equation 32 also shows that $|\nabla \psi|$ represents (roughly speaking) surface proximity or closeness, i.e. the surfaces are 'close' when $|\nabla \psi|$ is large, and farther away when it is small.

The wave-vector quantity introduced in section two, $S = \theta - \iota(\zeta - \zeta_k)$, the curvatures, and the local shear are coupled by the integrated local shear, defined as

$$\Lambda = \frac{\nabla S \cdot \nabla \psi}{B}. \quad (33)$$

To see that Λ represents the integrated local shear, we use $\mathbf{B} = \nabla \psi \times \nabla S$ and 33 in 24 to get

$$s = -\frac{g^{\psi\psi}}{B^2} \mathbf{B} \cdot \nabla \frac{\Lambda B}{g^{\psi\psi}}. \quad (34)$$

In field aligned coordinates we then have

$$\Lambda = -\frac{g^{\psi\psi}}{B} \int_{\eta_k}^{\eta} d\eta \sqrt{g} \frac{B^2}{g^{\psi\psi}} s. \quad (35)$$

The integration constant η_k gives the value along the field line where the integrated local shear is zero.

The integrated local shear is directly related to the coefficient D . Using the expression for D and 33 a direct calculation shows

$$\frac{\Lambda B}{g^{\psi\psi}} = -D - (\zeta - \zeta_k) \iota', \quad (36)$$

(29) where $\iota' = d\iota/d\psi$ is the global shear (or simply shear). Employing this expression in 34 yields

$$s = \frac{g^{\psi\psi}}{B^2} \left(\frac{\iota'}{\sqrt{g}} + \mathbf{B} \cdot \nabla D \right). \quad (37)$$

Employing 37 in 25 and flux surface averaging, we find

$$l' = \frac{V'}{4\pi^2} \left(\sigma \langle \frac{B^2}{g\psi\bar{\psi}} \rangle + p' \langle \lambda \frac{B^2}{g\psi\bar{\psi}} \rangle - 2 \langle \tau_n \frac{B^2}{g\psi\bar{\psi}} \rangle \right). \quad (38)$$

Equations 25, 37 and 38 show that the field curvatures are intimately related to the surface currents; the currents literally turn the field about the surface. The relation 37 shows that the local shear has a similar physical interpretation as the global shear, except varying point to point and with a sign difference. It also shows that the integrated local shear behaves quantitatively like the integrated global shear (on average).

C. Relation to instability quantities

We may use the identity $\mathbf{B} = \nabla\psi \times \nabla S$ to find the relations relevant for the instability modeling. By orthogonal decomposition on the wavevector and using definition 33, we have

$$\mathbf{k} = k_\alpha \frac{B}{|\nabla\psi|} (\hat{\mathbf{b}} \times \hat{\mathbf{n}} + \Lambda \hat{\mathbf{n}}). \quad (39)$$

Thus, as an observer moves along a field line, away from the point of minimum integrated local shear, the wavevector stretches out in the normal direction to the surface, with an amount of stretching proportional to the net (i.e., integrated) local shearing of the field. This stretching out of the wave-vector is evidently a wave dispersion effect associated with the magnetic medium, impeding propagation across the longer scales of a field line domain.

The instability analysis terms 7, 8 for use in 14 may now be expressed using the manifestly geometrical expressions. Using 16 and 39 the vector parts of the ∇B and curvature drift become $\frac{\hat{\mathbf{b}} \times \nabla B}{B} \cdot \nabla \hat{\phi} = ik_\alpha \left(\frac{B}{|\nabla\psi|} (\kappa_n - \kappa_g \Lambda) - \frac{\mu_0 p'}{B} \right) \hat{\phi}$, $\hat{\mathbf{b}} \times \kappa \cdot \nabla \hat{\phi} = ik_\alpha \left(\frac{B}{|\nabla\psi|} (\kappa_n - \kappa_g \Lambda) \right) \hat{\phi}$. We also have that $k_\perp^2 = k_\alpha^2 \frac{B^2}{g\psi\bar{\psi}} (1 + \Lambda^2)$.

The normalized instability terms thus take the form

$$\hat{\omega}_d = 2L_d^2 B_0 \frac{\kappa_n - \Lambda \kappa_g}{|\nabla\psi|} - L_d^2 B_0 \frac{\mu_0 p'}{B^2}, \quad (40)$$

$$\hat{k}_\perp^2 = L_k^2 B_0^2 \frac{1 + \Lambda^2}{|\nabla\psi|^2}. \quad (41)$$

These are the rigorous versions of the oft-mentioned low-beta scalings for a tokamak, where $\kappa_n \sim -\cos\theta$, $\kappa_g \sim \sin\theta$, $\Lambda \sim \hat{s}\theta$, gives $\hat{\omega}_d \sim -(\cos\theta + \hat{s}\theta \sin\theta)$ and $\hat{k}_\perp^2 \sim 1 + \hat{s}^2\theta^2$.

D. Straight field line coordinate modeling

Next we discuss modeling of the straight coordinates $\theta(\mathbf{r})$, $\zeta(\mathbf{r})$. Instead of specifying \mathbf{x} directly in terms of the straight field line coordinates, we specify $\mathbf{x}(\bar{\theta}, \bar{\zeta})$ where $\bar{\theta} = \bar{\theta}(\theta, \zeta)$, and $\bar{\zeta} = \bar{\zeta}(\theta, \zeta)$ as a clarifying notational

choice. Equation 27 as well as the jacobian, etc. are then computed using the chain rule. Formally, these coordinate mappings are determined by the global MHD equilibrium problem, with the transformation taking the form $\bar{\theta} = \sum_{mn} \bar{\theta}_{mn} \sin(m\theta - n\zeta)$ with $\bar{\theta}_{00} = 1$ to preserve periodicity. As opposed to solving the global problem, we would like to take a simple modeling choice such as $\bar{\theta} = \theta$, $\bar{\zeta} = -\phi$, where ϕ is the standard toroidal coordinate. This was the choice made in²⁴ which we employ in all the primary results and clarify below.

To make things more concrete, say we were to parametrize $\mathbf{x}(\theta, \zeta)$ directly, i.e. as $\bar{\theta} = \theta$, $\bar{\zeta} = \zeta$, such that $\mathbf{x}(\theta, \zeta) = (\sum_{mn} R_{mn} \cos(m\theta - n\zeta)) \mathbf{e}_R(\phi) + (\sum_{mn} Z_{mn} \sin(m\theta - n\zeta)) \mathbf{e}_Z$, where $\mathbf{e}_R(\phi)$ is a toroidal basis vector ($\mathbf{e}_R(\phi) = \cos\phi \hat{\mathbf{x}} + \sin\phi \hat{\mathbf{y}}$) and similarly $\mathbf{e}_Z = \hat{\mathbf{z}}$. In order to compute 27, the parametrization $\phi(\theta, \zeta)$ must also be known. We can define the surface itself as that collection of points $\{\mathbf{x}(\theta, \zeta) \text{ s.t. } \theta, \zeta \in [0, 2\pi]\}$. Any reparametrization of the surface $\mathbf{x}(\bar{\theta}, \bar{\zeta}) = \mathbf{x}(\bar{\theta}(\theta, \zeta), \bar{\zeta}(\theta, \zeta))$ for which $\bar{\theta}$ and $\bar{\zeta}$ are periodic in $[0, 2\pi]$ will give the same collection of points \mathbf{x} .

We can show that the initially arbitrary coordinates $\bar{\theta}, \bar{\zeta}$ are trigonometrically constrained by the surface mapping, i.e. they become related to geometric coordinates as soon as a shape is specified. Say we decompose the surface mapping into the vector from the origin to the magnetic axis, and the vector from the axis to a point on the surface, $\mathbf{x}(\bar{\theta}, \bar{\zeta}) = \mathbf{x}_a + \mathbf{x}_s$. Here, because \mathbf{x}_a only references a curve, it may be parametrized by a single variable, i.e. we may find a parametrization $\mathbf{x}_a = \mathbf{x}_a(\phi(\bar{\zeta}))$. (The magnetic axis mapping \mathbf{x}_a only consists in the fourier harmonics of index $(m, n) = (0, n)$.) A straightforward definition for the geometric cross sectional angle $\theta_g = \theta_g(\bar{\theta}, \bar{\zeta})$ may be taken as $\tan\theta_g = \frac{(\mathbf{x} - \mathbf{x}_a) \cdot \mathbf{e}_Z}{(\mathbf{x} - \mathbf{x}_a) \cdot \mathbf{e}_R}$. Assuming the mapping $\bar{\zeta} = \bar{\zeta}(\phi)$ is specified, then this definition immediately constrains the geometric meaning of $\bar{\theta}$.

Take the example of an idealized circular cross section tokamak. We may write $\mathbf{x} = (R_0 + \rho \cos\bar{\theta}) \mathbf{e}_R(\phi) + \rho \sin\bar{\theta} \mathbf{e}_Z$, and choose $\zeta = -\phi$. Then, using \mathbf{x} in the previous definition, one finds $\theta_g = \bar{\theta} + N\pi$, where N is an integer. Thus the initially suggested modeling choice of $\bar{\theta} = \theta$ actually corresponds to taking the straight field line angle to be identical (for a circular tokamak) to the geometric angle.

Without actually solving $\mathbf{J} \times \mathbf{B} = \nabla p$ for the coordinate transformations, we do not know how inaccurate this guess turns out to be. In a high aspect ratio tokamak geometry, it is possible to derive conditions on $\bar{\theta}(\theta)$, but in a stellarator, is generally analytically intractable to determine $\bar{\theta}(\theta, \zeta)$ and $\bar{\zeta}(\theta, \zeta)$. Thus for the remainder of the paper we will mainly focus on the simplistic choice $\bar{\theta} = \theta$, $\bar{\zeta} = \zeta$, understanding that this modeling convenience must be kept in mind and potentially modified in the future. Furthermore, we always take the conventional choice $\bar{\zeta} = -\phi$, which avoids significant complications since the partial derivatives of \mathbf{e}_R with respect to θ and ζ become trivial. In this notation, the field al-

ways goes clockwise around the torus when viewed from above, while twisting clockwise poloidally around it when viewing along the field.

In axisymmetry, the coordinate transformation choice for $\bar{\theta}$ is closely related to the variation in poloidal field strength $B = B(\theta)$ and the surface proximity $|\nabla\psi| = |\nabla\psi|(\theta)$. This is easy to see for the magnetic field strength since (with 28 showing \sqrt{g} to be independent of $\partial\bar{\theta}/\partial\theta$), the ‘‘poloidal’’ component of the magnetic field from 27, $\iota\partial\mathbf{x}/\partial\theta/\sqrt{g}$, scales linearly with the coordinate transformation, $\iota\partial\mathbf{x}/\partial\theta/\sqrt{g} = \iota(\partial\mathbf{x}/\partial\bar{\theta})\partial\bar{\theta}/\partial\theta/\sqrt{g}$. The explanation is similar for the surface proximity since $\nabla\psi = (\partial\mathbf{x}/\partial\theta \times \partial\mathbf{x}/\partial\zeta)/\sqrt{g}$.

This feature is similar to that of the the local 2-D formulation of Miller et. al.^{42,45}. There, the poloidal field strength is written down first, consistent with the flux surface shape and the equilibrium coordinates, and then the radial shaping coefficients that arise are assumed to be known, or estimated asymptotically. The difference in the local 3-D formulation is that the covariant basis vectors for the field are employed instead of the contravariant vectors, so that the coordinate mappings that arise have no radial parametrizations to be specified. In both cases, freedom in the coordinate parametrizations – either radial, in the case of 2-D, or straight field line angle, in the case of 3-D – manifests itself as freedom in the surface distribution of field strength B and surface proximity $|\nabla\psi|$.

IV. MODELING VALIDITY

In order to determine the validity of the local equilibrium (LEQ) modeling and input for the GENE/GIST code, it was necessary to perform checks against other, established equilibrium models, such as VMEC, the $\hat{s} - \hat{\alpha}$ model, and also single parameter shaping scans. These checks are detailed below.

A. Comparison of VMEC and LEQ geometry

We first compare VMEC⁹⁷ generated circular tokamak equilibrium data with two analogous LEQ cases, with the field line properties shown in Figure 1. The LEQ cases are chosen with the same bulk geometry parameters ($\rho/R_0 = 0.2, \iota = 1.48, \hat{s} = 1.34, \hat{\alpha} = 0.025$) as the VMEC case but with two values for the straight field line transformation, $\bar{\theta}(\theta)$. The first of these uses $\bar{\theta} = \theta + 0.3 \sin \theta + 0.03 \sin 2\theta + 0.003 \sin 3\theta$ to give excellent agreement with VMEC results. The second uses $\bar{\theta} = \theta$, giving mostly good agreement except in the quantity g^{11} (top left of Figure 1). The necessity of parametrizing $\bar{\theta}$ to give best agreement with the global equilibrium VMEC calculation is evidently due to the fact that in the VMEC calculation, the outboard poloidal field strength (and flux surface proximity) must be increased roughly 30% from

the inboard, due to the well known effect of the Shafranov shift; this effect is precisely what the change to the $\bar{\theta}$ parametrization accomplishes.

B. Comparison of $s - \alpha$ and LEQ geometry instability

Next, growth rates (eigenvalues) were calculated for the built-in GENE $\hat{s} - \hat{\alpha}$ model at code parameters SHAT, AMHD, TRPEPS, MAJOR_R, $Q_0 = \{1, 0, 0.2, 1.0, 1.484\}$ and compared with a circular tokamak LEQ case with similar parameters, $\hat{s} = 1, \hat{\alpha} = 0.05 \sim 0, \iota = 1/1.484 = 0.675, \rho/R_0 = 0.2$. The resultant spectra are shown in Figure 2. The LEQ model and $\hat{s} - \hat{\alpha}$ model are substantially different (the latter being much less generic) and provide different geometric data for input to the GENE calculations; for review of the $\hat{s} - \hat{\alpha}$ model, one may see e.g.^{98,99}. Figure 2 indicates good qualitative agreement between the models considering these differences, enough to establish the validity of the results.

The initial calculations for Figure 2 revealed that it was crucial to choose the right normalization constants for the normalized GENE/GIST inputs to benchmark successfully with the $\hat{s} - \hat{\alpha}$ results. For the rest of the paper, we employ the GIST normalizations which gave comparable geometric element magnitudes (when viewed in the GENE IDL diagnostic) to the built-in $\hat{s} - \hat{\alpha}$ model.

C. Elementary parameter scans

Next the results of several basic parameter scans are presented for a circular tokamak surface and an elliptical cross section surface, with parametrization $R = R_0 + \rho_R \cos \bar{\theta}, Z = \rho_Z \sin \bar{\theta}$, with ellipticity defined as $e = \rho_Z/\rho_R$. Equilibria were generated and solved with base parameters $\epsilon = \rho/R_0 = .1, 1/L_n = 2, 1/L_T = 10, \tau = 1, \hat{s} = 1, \hat{\alpha} = 0.025, \iota = 0.675$, and then scans were performed in aspect ratio, ellipticity, and also the global shear parameter, with the last case being performed with both VMEC and without the VMEC based $\bar{\theta}$ parametrization. These results are shown in Figure 3.

The growth rates increase with aspect ratio in the range scanned, and also with ellipticity. The shear can be seen to be stabilizing, with negative shear being more stabilizing than positive shear, and the case with VMEC parametrization being more unstable than the case without. The scaling of growth rates with ellipticity has been studied on several occasions, and increasing elongation has been found to have a stabilizing effect³³. In contrast, the increase in ellipticity here is destabilizing.

There are a number of ways to explain this discrepancy. Firstly and probably most importantly, the poloidal field strength parametrization $\bar{\theta} = \theta$ is kept constant in our scan, whereas in the Miller type scans as in³³ it is adjusted simultaneously with the surface deformation. Furthermore the shear scan in Figure 3 reinforces how the field strength parametrization can have a nontrivial effect

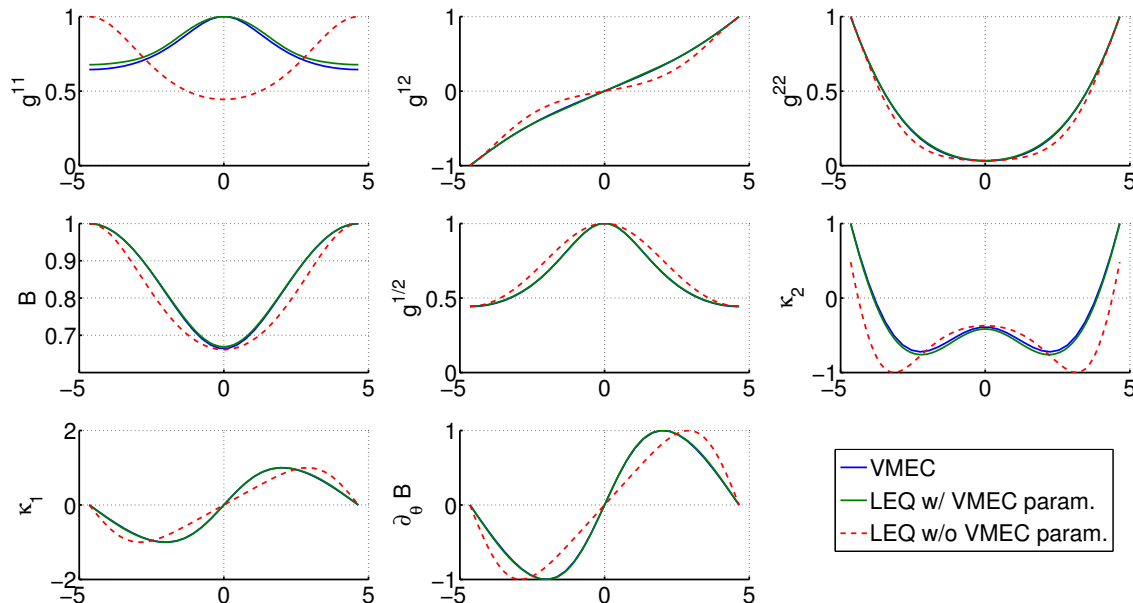


FIG. 1. Comparison of equilibrium data for a VMEC circular tokamak calculation with LEQ circular tokamak calculations. The x-axis indicates a $\theta \in [-\pi, \pi]$ or $\eta \in [-\pi/\iota, \pi/\iota]$ domain along a field line, centered at the outboard midplane. The green curve shows an excellent match with the VMEC parameters for the $\bar{\theta}$ transformation given in the text, whereas the red curve with $\bar{\theta} = \theta$ does not well match the g^{11} element, but matches all the rest. All quantities here are normalized to one as their absolute magnitudes are generally subject to independent normalization factors in the different codes.

on the growth rate scalings. The importance of the field strength scaling with shape deformation has also been noted in several other references^{34,39,100}. We therefore conclude that the neglect of this effect is what causes the difference in the elongation scaling from prior results. In any case, the difference in this trend should not be taken to invalidate the present results, which are chiefly concerned with understanding the instability's relation to the geometry – whatever that geometry may be.

V. RESULTS AND ANALYSIS

In this section we present the results of calculations and analysis using the combined modeling framework given above. First we investigate selective geometry variations across three separate sequences of configurations. The first set consists of 2-D configurations, whereas the second and third set are 3-D. The parametrizations of these shapes are placed in a separate appendix. We first discuss the motivation behind these choices. Secondly we discuss how the geometry properties can be best understood, given the profuse amount of geometric data involved. Next we show how the analytic models of section two give reasonable agreement with results from GENE in the maximum linear growth rates. We discuss how the curvature and polarization terms control the growth rates in accordance with the analytic theory. Finally we

comment on the interesting numerical and analytic mode structure features. Lastly, we discuss general qualitative and quantitative features evident from study of the instability properties of the different geometries, and how they may be understood.

The linear growth rate spectra for each of the selected geometries were calculated using GENE, as well as the analytic model of equation 14 using the gaussian eigenfunction methodology discussed in section two. The GENE spectra were calculated over the range $k_{\alpha}\rho_{th} \in 0.1, 0.2, \dots, 1$, and the analytic spectra in the range $k_{\alpha}\rho_{th} \in 0.01, 0.02, \dots, 1$. The input parameters for the calculation were: $L_n^{-1} = 2, L_T^{-1} = 20$, such that $\eta_i = 10$ and the cases are far from marginality, $\gamma \sim O(1)$. The temperature ratio was set as $\tau = 1$. The resolutions used in the GENE calculations are minimally $[\text{nspec}, \text{nx0}, \text{nky0}, \text{nz0}, \text{nv0}, \text{nw0}] = [1, 16, 1, 64, 32, 16]$ for the 2-D cases, with the parallel resolution nz0 increased to 128 for the 3-D cases, which have much more variation in the parallel spatial direction. Resolution scans indicated that the all cases were sufficiently resolved for convergent results.

We recall the flux tube method of solution via GENE which we employ here involves periodic boundary conditions on a finite domain, typically $\theta \in [-N\pi, N\pi]$, where $N = 1$ in this study, rather than WKB-like boundary conditions on an extended domain, as is typically used in direct ballooning formalism calculations. The reason

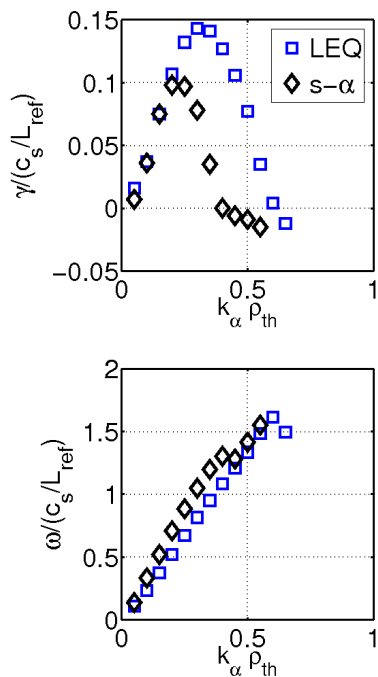


FIG. 2. Comparison of GENE results using built-in $\hat{s} - \hat{\alpha}$ model and LEQ input (using the VMEC matched $\bar{\theta}$ mapping) into GIST. The parameter settings are $1/L_n \sim \text{OMN} = 1$, $1/L_T \sim \text{OMT} = 6$, $\tau = 1$, with adiabatic electrons. The spectral dependence shows the well known inverted parabola type behaviour as discussed in section two. The quantitative differences between the two curves are reasonable considering the differences between the $\hat{s} - \hat{\alpha}$ and LEQ models – interested readers may consult similar comparisons in⁴⁰.

why the geometric coefficients are the same in the two approaches was well discussed by Beer et. al.⁸¹. In the analytic calculations presented here, the domain is cut off at finite length by the choice of the finite length eigenfunction. The validity of the flux-tube approach is an interesting yet often complicated subject and has been considered in multiple references^{49,79,80,82,101}.

A. Selection of specific geometries

In this section we present three sets of configurations, with equilibrium parameters summarized in table I and with $\hat{\alpha} = 0.025$, sufficiently small to disregard pressure gradient effects. The shaping parametrizations for these cases are given in the Appendix. The shaping sequences are selected so that the length scale constant L_\perp (minor radius) remains constant within the sequence, with the exception of case t3, which has a somewhat enlarged aspect ratio. Otherwise, it would not be possible to distinguish differences in the shaping from differences in the aspect ratio or gross configuration parameters.

The geometries were selected to pick out diverse features of 2-D and 3-D shaping. An attempt was made to include canonical or simple cases, reflecting common

Case	L_\perp/R_0	ι	\hat{s}	N
t0	.2	.67	1.34	–
t1	.2	.67	1.34	–
t2	.32	.67	1.34	–
t3	.2	.67	1.34	–
t4	.2	.67	1.34	–
sa0	.14	0.9	-.27	6
sa1	.14	0.9	-.11	6
sa2	.14	0.9	-.27	6
sa3	.14	0.9	-.77	6
si0	.16	0.9	-.14	5
si1	.16	0.9	-.033	5
si2	.16	0.9	-.036	3

TABLE I. Table of basic parameter settings for equilibrium cases, including the case label, transform, global shear, and field period. The first five cases labeled with a ‘t’ are axisymmetric cases, whereas the cases labeled with ‘s’ are non-axisymmetric.

features, as well as shapes with modifications to those essential features, and shapes with modifications in essential analytic geometric qualities, such as whether the cross section merely rotates (in 3-D) in the toroidal direction, or both rotates and deforms; the more technical nature of these terms will be discussed below. Some care was also taken to select geometries with $\iota \sim 1$, as for $\iota \gg 1$, the shaping tends to be unrealistically strong, whereas for $\iota \ll 1$, the field line samples many $|B|$ wells on the outboard side of the torus, leading to effective dominance of trapped ion modes in GENE calculation results, outside the scope of the present study.

The tokamak cases were selected as follows. Cases t0 and t1 are standard circular torii, but case t0 uses a coordinate parametrization $\bar{\theta} = \theta + 0.3 \sin \theta + 0.03 \sin 2\theta + 0.003 \sin 3\theta$ selected to match an analogous equilibrium generated from VMEC. All other cases use the simplified assumption $\bar{\theta} = \theta$. Case t2 employs a D-shaped parametrization with elongation and triangularity, relevant to theoretical and experimental shaping in cases like the spherical tokamak. Case t3 has been shaped to become concave outboard, whereas case t3 is concave inboard. The cross sections are shown with their geodesic curvature distribution in Figure 4. Note how the last two cases take on a doubled period of geodesic curvature variation due to the introduction of a concave region.

In selecting the stellarator cases, the procedure was generally to fix the geometry to a convergent solution to equation 28, and then modify \hat{s} such that $\sigma \approx 0$, such that the equilibria were genuinely stellarator-like. The stellarator cases sa0-sa3 consist in a simple scan over triangularity, with the triangularity parameter fixed as $\rho_3 = \{\rho_2/10, 0, -\rho_2/10, -2\rho_2/10\}$, respectively; case sa1 has only pure elongation shaping.

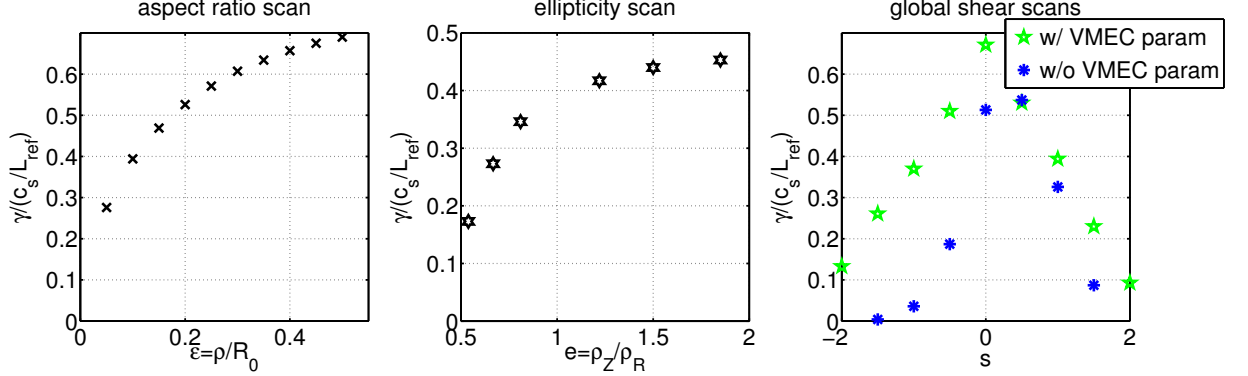


FIG. 3. Scans of elementary shaping parameters on circular and elliptic tokamak LEQ cases.

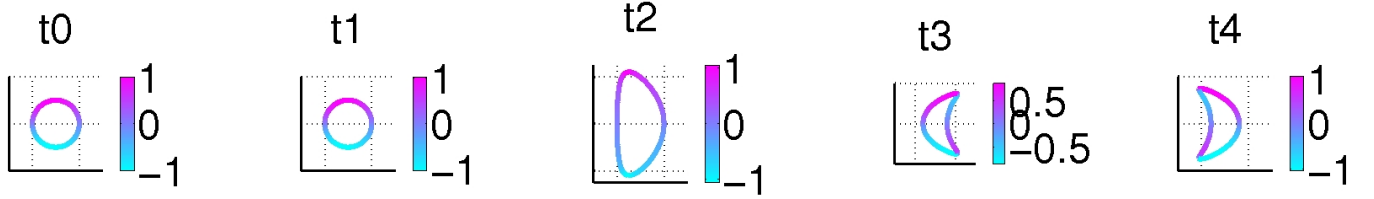


FIG. 4. κ_g (geodesic curvature), cases t0,t1,t2,t3,t4. Direction towards the inboard is to the left.

These cases are examples of ‘rotational’ 3-D shaping in that the cross sections *only* rotate poloidally about the magnetic axis along the toroidal direction. Purely rotating geometries may be seen as canonical cases for the stellarator, similar to the canonical circular tokamak cases t0 and t1. Purely rotational shaping cases may be contrasted with those involving ‘deformational shaping’, where the cross section changes both orientation and shape in the poloidal plane.

To be more concrete about the meanings of rotation, deformation, and translation, we discuss how they are parametrized. If the surface is parametrized e.g. as $R = \sum R_{m,n} \cos(m\theta - n\zeta)$ and $Z = \sum Z_{m,n} \sin(m\theta - n\zeta)$ (e.g., see Appendix), then translational shaping harmonics are those of $R_{0,n}, Z_{0,n}$. Rotational harmonics are those consisting in $R_{m,n}, Z_{m,n} = -R_{m,n}$, however, with the necessary condition $R_{1,0}, Z_{1,0} > R_{m,n}$. Harmonics with integer multiples, e.g. $R_{2m,2n}, Z_{2m,2n}$ do not rotate at the same rate or with the same shape, it should be noted. Deformational shaping is induced by combinations of different rotational harmonics with unmatched rates of toroidal rotation. For purposes of completeness

we also note that the $R_{0,0}$ and $Z_{0,0} = 0$ (without loss of generality) reflect the major radius, and the $R_{m,0}, Z_{m,0}$ are just those that categorize the 2-D poloidal shaping.

The cross sections of cases sa0, sa1, sa2, sa3 are very simple and omitted. The cross sections of cases si0-si2 are shown in Figure 5. These were selected to contribute increasing amounts of deformation; case si2 actually has a reduction in field period from case si0 and si1 in order to keep the rotational transform fixed as the poloidal shaping was increased.

B. Analysis of geometric properties

A great deal of geometric information is associated with each case. In this section we elaborate how the geometric data may be most fully but also concisely understood. In principle, all the information relevant to the instability is contained within the surface quantities of $B, |\nabla\psi|, \sqrt{g}, \kappa_n, \kappa_g, \tau_n$, as well as the equilibrium parameters of ι, p' , and the currents σ , which can be crucial to the local shear. Some simplifications are possible here;

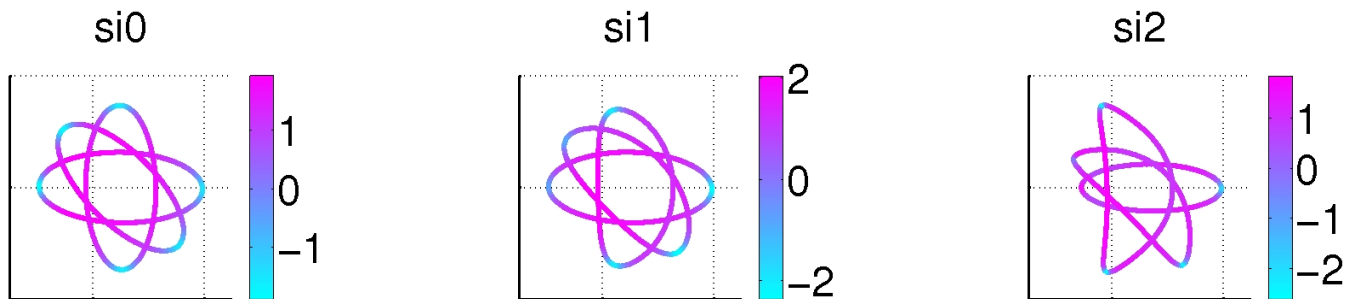


FIG. 5. τ_n (normal torsion), cases si0,si1,si2. Direction towards the inboard is to the left. Three cross sections are shown from half of a field period.

for the stellarator cases $\sigma \approx 0$ by construction, meaning the local shear is simply related to the torsion (equation 25). We also find in general in the present study that \sqrt{g} and B have a lesser role than the other quantities.

We analyze the geometric data using four principal methods. The first is by field line geometric plots, which are most directly quantitatively relevant to the drift and polarization coefficients (which determine the instability properties, as described in section two). These are shown for the tokamak cases in Figure 6. The plots contain the geometric data in one poloidal circuit (centered about $\theta = 0$ on the outboard midplane), the same as the modeled gaussian eigenfunction full-width.

For 2-D configurations, the field line plots are effective at characterizing the entire geometry, since a single field line is representative of the entire toroidal circumference. The normal curvature is typically always simply bad (negative) on the outboard, and the torsion generally always positive, since the nonzero net currents turn the field in a uniform direction. The geodesic curvature, on the other hand, is subject to modification depending on surface convexity or concavity (with respect to the field). For 3-D configurations, the field line plots tend to be more complicated, and characterized by many more zero crossings, as for say $\iota \sim 1$ and a moderate field period, say $N = 5$, there will be at least 5 oscillations in the sign of the normal curvature, as the field line passes over the helical ridge (assuming the helical curvature is dominant).

Furthermore, at least two points on the outboard midplane must be used to fully characterize the instability properties of a 3-D surface. For the case labeled ‘si’, we choose the toroidal positions on the outboard midplane where κ_n is most negative, and where κ_n is least negative, i.e. at the beginning and middle of a field period ($\zeta = 0$ and $\zeta = \pi/N$ with $R \sim \cos(\theta - N\zeta)$). The latter, ‘oblate’ cases are appended with the letter ‘b’, e.g. si0b, si1b, si2b. The field line properties vary continuously when moving between such extremals, so that these points are then broadly characteristic of the outboard geometry. For the simpler cases sa0, sa1, sa2, sa3, we only analyze the instability properties at the oblate outboard points.

Secondly, it proves helpful to use 3-D geometric surface plots for 3-D configurations, with the field line (flux-tube) trajectory overlaid. These aid interpretation of the geometric causation of the field line plot information. For example, Figure 7 shows the field line geometry for the purely rotational stellarator cases sa0-sa3; the 3-D geometric surface plots in Figure 8 show that the oscillatory patterns in the data are simply due to the field line transcribing helical ridges over the surface.

We thirdly make use of two-dimensional cross section plots, as already shown in Figures 4 and 5. These are indispensable for understanding the way the cross section changes toroidally. Overlays of the curvatures or other geometric elements also greatly clarify how the signs of the curvatures are determined by the geometric shape. Lastly, we also sometimes make use of 2-D surface plots of the geometric data. These can be useful for picking out qualitative features of the geometry which are not apparent from the other methods, as particularly for case si2 in the present study.

The field line geometric properties for rotational and deformational stellarator cases si0, si1, si2 are shown in Figure 9 and for si0b, si1b, si2b in Figure 10. The field line plots for the case with the most rotation and deformation (si2), Figures 9, 10, show geodesic curvature and torsion with unusual behavior, which remains almost single signed for the entire poloidal field period. This is partly simplistic, due to the reduced field period of case si2 compared to si0 and si1 ($N = 3$ compared to $N = 5$), but more surprisingly, it also controlled by the specific shaping. (However, the effects cannot be fully separated since it is the increase in the shaping which allows N to be reduced (keeping ι fixed), while retaining a convergent equilibrium solution.)

The grossness of this effect is identified from examination of the 2-D surface data, as shown in Figure 11, comparing the 2-D surface distributions of κ_g for cases si0, si1, si2. As shown there, the helical curvature is notably tuned out for the shaping parametrization of case si2. That case’s qualitative geometric behavior is arguably more like a tokamak than a traditional stellarator, since the symmetries are almost up/down and left/right.

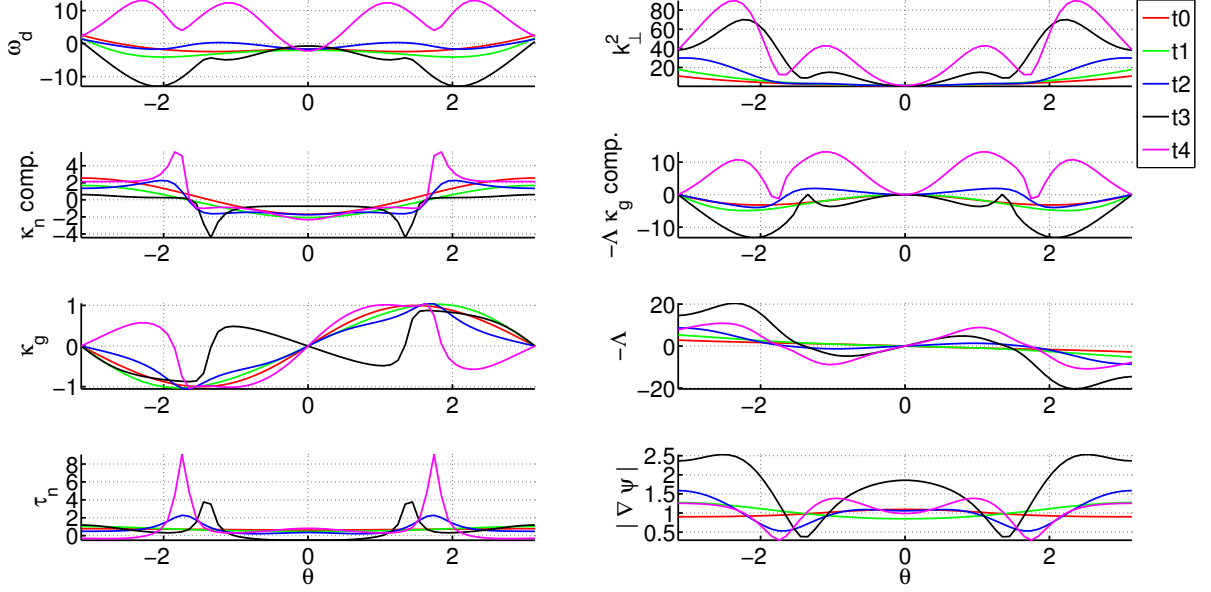


FIG. 6. Field line geometric plots, cases t0,t1,t2,t3,t4. The κ_n and $-\Lambda\kappa_g$ components refer to the first and second terms of equation 41 (including the denominator and pre-factors).

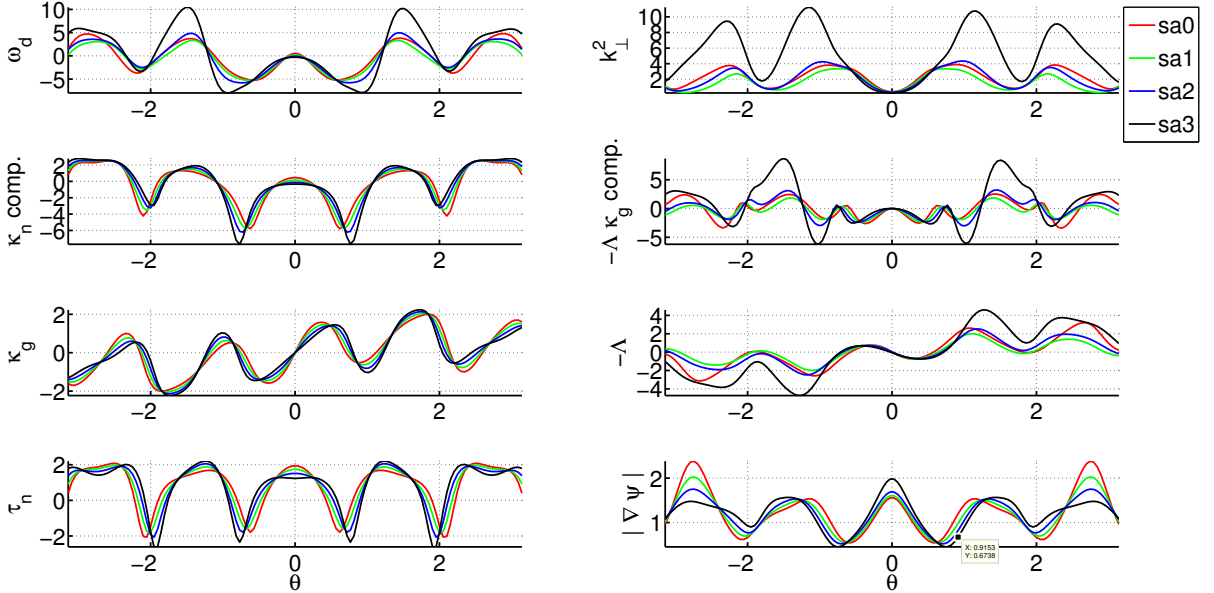


FIG. 7. Field line geometric plots, cases sa0, sa1, sa2, sa3.

C. Linear growth rate calculations

The maximum linear growth rates from the four sets of equilibria (two outboard points for cases ‘si’) are shown in Figure 12. Before discussing the results in detail, we men-

tion some features which are generally apparent. First, the spectra from the analytic model are generally much more simple than the spectra calculated in GENE. They appear (roughly speaking) as an inverted parabola centered around $k_\alpha \rho_{th} \sim 0.3 - 0.5$. The GENE spectra typ-

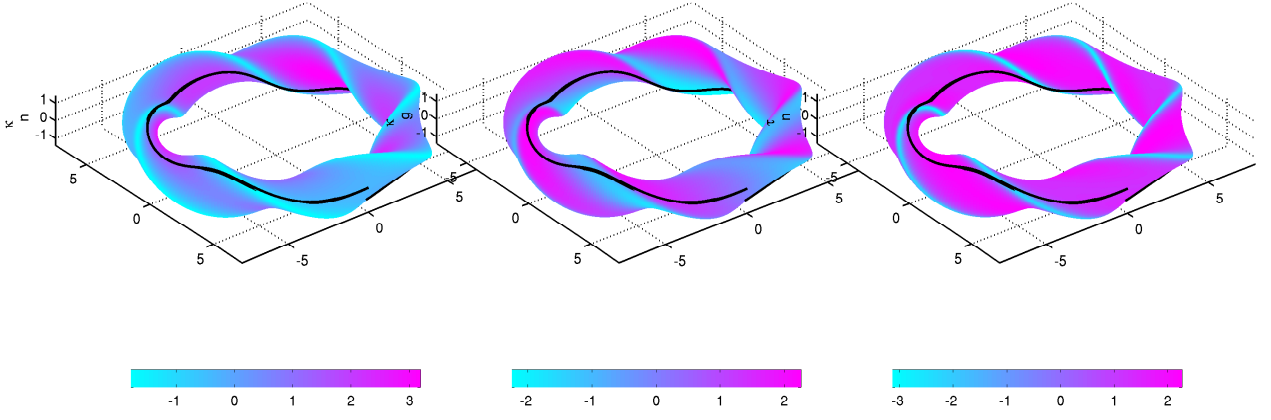


FIG. 8. $\kappa_n, \kappa_g, \tau_n$ (left to right), three dimensional geometric plots for case sa3.

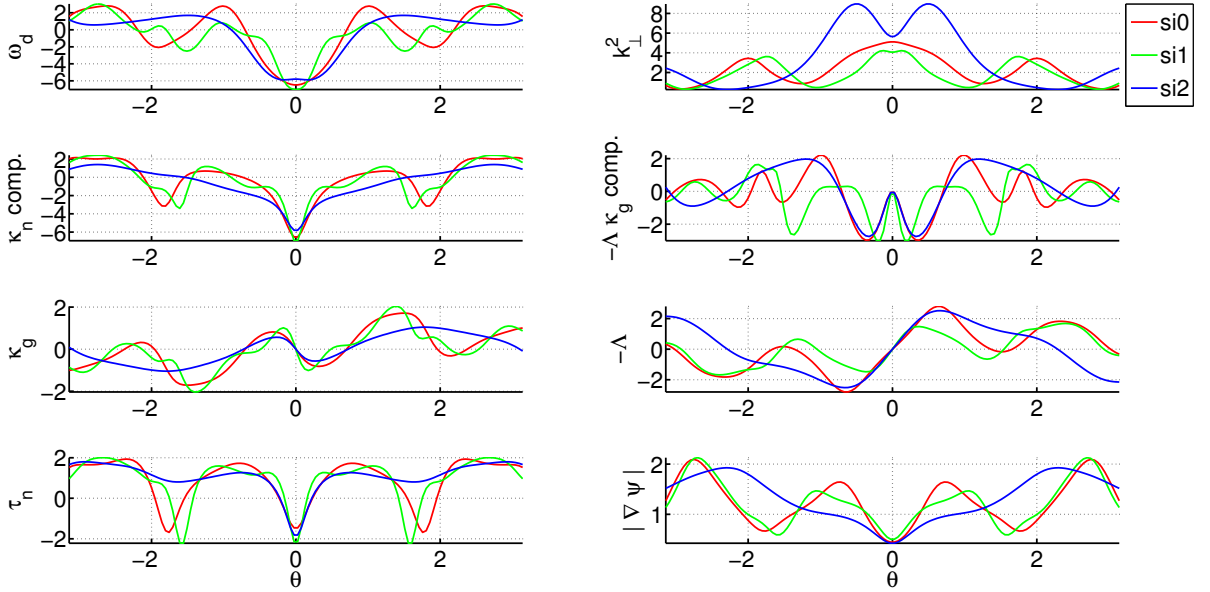


FIG. 9. Field line geometric plots, cases si0, si1, si2. The field line domain shown here originates from the point on the outboard midplane with maximal radial excursion (the prolate point).

ically extend to higher $k_\alpha \rho_{th}$ and show more elaborate structure. Secondly, the analytic model consistently overpredicts the GENE results. This may suggest that the kinetic effects are overall stabilizing when incorporated into the calculations. Despite these differences, based on

the results shown in Figure 12 and in many other sets of calculations, the analytic model results show consistent agreement in trend with the GENE calculations. Agreement between the analytic model and GENE lends substantial justification to the argument that the drift and

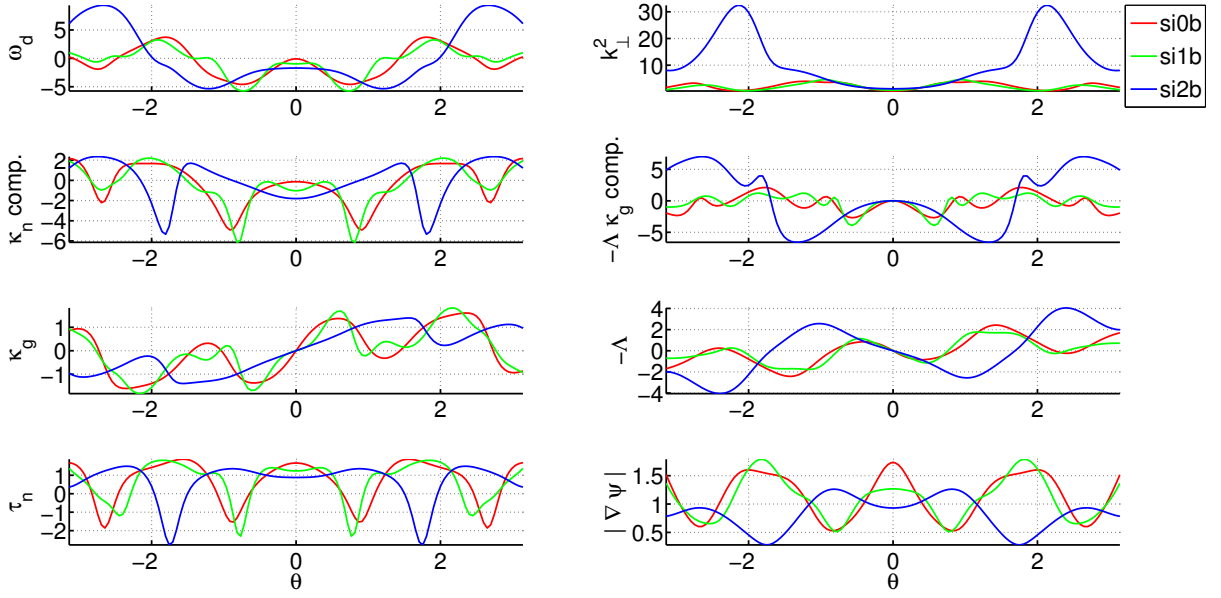


FIG. 10. Field line geometric plots, cases si0b, si1b, si2b. The labels are appended with the letter ‘b’ to indicate that the field line domain shown here originates from the point on the outboard midplane with minimal radial excursion (the oblate point).

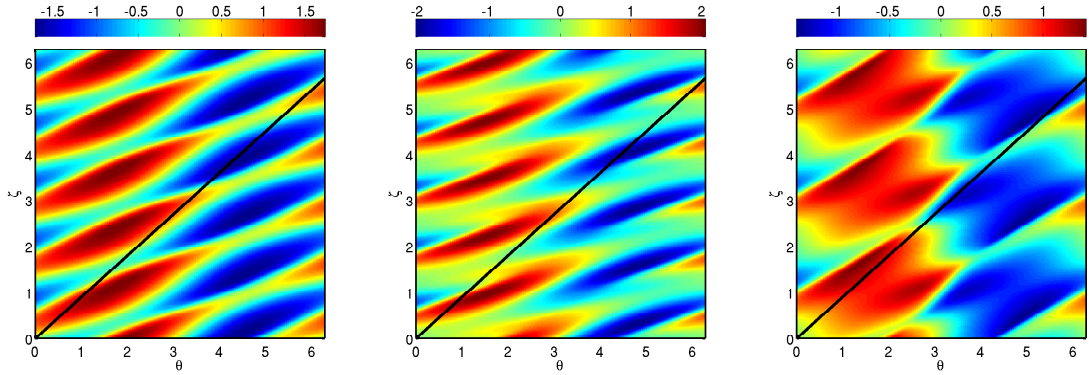


FIG. 11. κ_g (geodesic curvature), cases si0b, si1b, si2b. Geodesic curvature in a typical, rotating cross section stellarator like si0b switches sign along any given fixed toroidal angle. For case si2b, the geodesic curvature breaks this symmetry and is most often single signed. The sign distribution is primarily top/bottom and left/right, as in a tokamak. A field line trajectory ($\iota = 0.9$) on the surfaces is shown.

polarization coefficient, and more precisely, their specific form of dependence on their subsidiary terms, are what chiefly control the magnitude of the instability, at least in this parameter regime far from marginal stability.

The general agreement in trend is well shown in Figure 12. For the 2-D cases (top left), the only place where the trend of the analytic model does not match the GENE trend is between cases t0 and t1, but there, the difference in analytic growth rates is slight. On case t3, the growth rate in the analytic model significantly over predicts the GENE growth rate, but this is an exception to most of the results seen in the investigation. It suggests the possibility of unusually strong kinetic effects for case t3, which may be plausible due to the highly enhanced polarization behavior of that case (see Figure 6, top right) forcing the mode to become more localized. For all other cases except case sa0 and sa2, the trends are also matched, and for cases sa0 and sa2 the difference in predicted growth rates is again very slight. Case t4 is predicted to be totally stable in the analytic model and nearly stable in GENE. This is due to the greatly reduced negativity of $\hat{\omega}_d$ and enhancement of \hat{k}_\perp^2 (as with case t3).

Given the geometric data plotted in Figures 6, 7, 9, 10, the results are somewhat self-explanatory with reference to the analytic model. However, a number of particular observations may be made on the detailed effects of the geometry. Firstly, in understanding the drastically improved polarization behavior and hence reduced instability of cases t3 and t4, the explanation is clearly due to the increase in the magnitude of Λ , which is in turn caused by a large increase in the magnitude of the local shear (not shown in Figure 6). This increase is not reflected uniformly in the torsion, suggesting it must be due to an increase in net currents, which indeed turns out to be the case. The reason why the currents are much larger for these cases will be clarified below.

Case t4 is distinguished from case t3 by a much more positive curvature drift coefficient $\hat{\omega}_d$. The reason for this is partly due to the increased magnitude in Λ , but also chiefly due to the reversal in the typical geodesic curvature polarity (sign) near $\theta \sim \pi/2$, which is achieved at the same position where Λ switches sign, thereby making the $-\Lambda\kappa_g$ contribution highly stabilizing. The fundamental alterations in the geodesic curvature distributions are well shown by Figure 4.

Rotational 3-D cases sa0, sa1, and sa2 have nearly the same stability, whereas case sa3 is significantly more stable. This is due to the improved polarization behavior (Figure 7, black curve), due to increased magnitude of Λ , which is essentially due to an increase in the average torsion or global shear (see Table I). Thus these cases reveal a typical global shear effect and not a particularly improved effect due to the local shaping. The increase in local shaping, however, is what itself allows the global shear to be higher, via relation 38, as will be discussed below.

Next we discuss the rotational and deformational shaping cases si0, si1, and si2. The points on the oblate loca-

tion of the outboard midplane with minimal radial excursion, designated 'b', are more unstable than the prolate points. This is a common characteristic seen in stellarator calculations in this investigation, which is surprising considering that the oblate points have better (more positive) normal curvature κ_n than the prolate points (si0, si1, si2). This could be caused by the simplified straight coordinate modeling approach but it could also well be a general characteristic. Regardless, it is notable that case si2 with the increased shaping (compared to si0, si1) manages to enhance the stability at the oblate point, while leaving the stability on the prolate point essentially unchanged. This demonstrates the possibility of changing the shaping to overall reduce the maximum instability level at not just one location, but the entire geometry.

On that note, it should also be noted that cases t3 and t4 were scanned for instability at the highly prolate poloidal positions near $\theta \sim \pi/2$, and found to have reduced instability there compared to the outboard midplane, meaning the standard picture of ballooning type modes peaking at the point of worst normal curvature κ_n may be shown to be oversimplified. The large degree of torsional (and hence polarization) shaping at those points compensates for the worsening in the normal curvature.

The improvement in stability of case si2b compared to si0b, si1b is clearly due to an improved polarization effect, not a curvature coefficient improvement. The polarization improvement is in turn due to increased magnitude of the integrated local shear. This itself is due to an increased connection length in the local shear, due to the notable single sign biasing of the torsion, as discussed in the previous subsection with respect to the geodesic curvature. However, it should also be noted that the minimum in $|\nabla\psi|$ is substantially reduced for case si2b, which can play a significant role in \hat{k}_\perp^2 due to the denominator going as $|\nabla\psi|^2$.

For completeness, the numerical spectra are shown in Figure 13. The stellarator spectra show more structure than those for the 2-D cases. The cases that are more stable have their maximum growth rates at lower b ; polarization stabilization, when strong, forces the modes to longer wavelengths where they are less unstable.

D. Observations on mode structures

It is interesting to note that agreement in analytic and numerical results is achieved despite a simplistic analytic assumption of a gaussian mode structure. Yet throughout the numerical results, with the exception of the 2-D cases, the modes in general *are not* observed to have a simple gaussian form. Furthermore, we note that although we make use of domains of single poloidal circuit width for the purposes of the results shown, we find that when the numerical GENE domain lengths are extended (by variation of the *n_{pol}* parameter and the geometry input), up to as many as 3 poloidal circuits, we find little

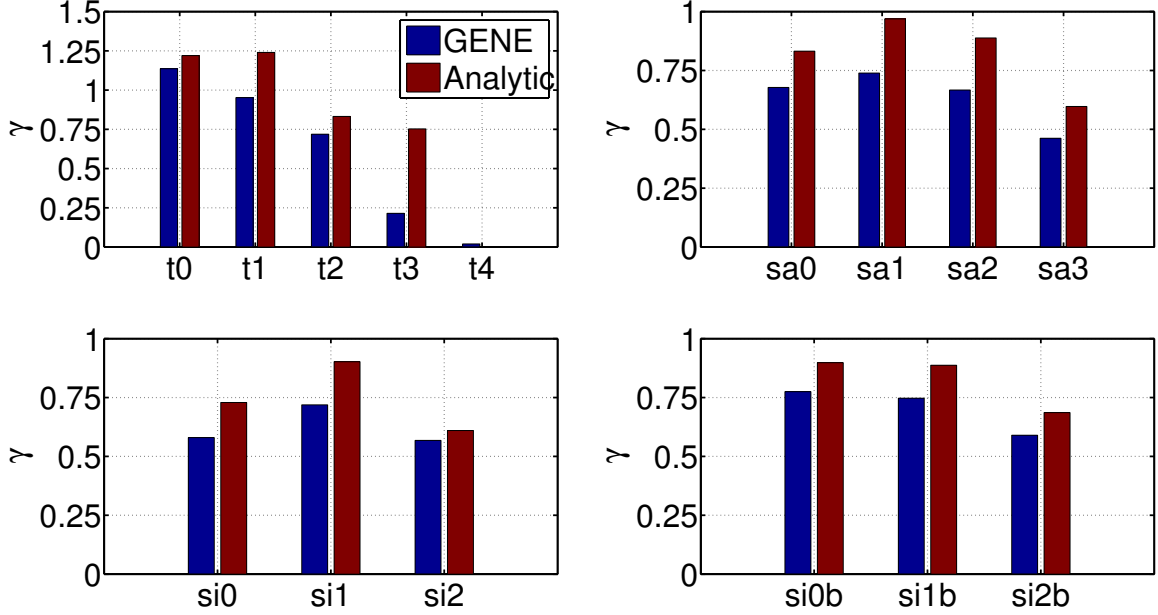


FIG. 12. Maximum linear growth rates (normalized by c_s/L_{ref}) for the cases selected for presentation, from both GENE (left most bars) and the analytic model (right most bars).

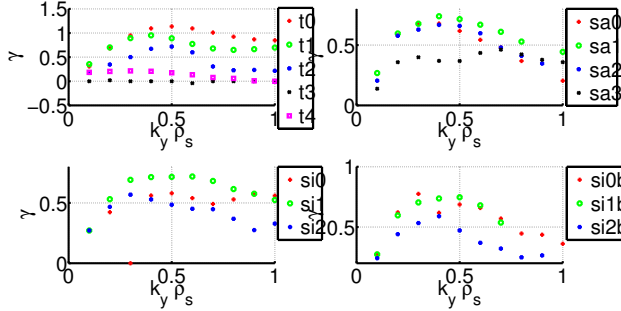


FIG. 13. Numerical linear growth rate spectra from GENE for cases scanned.

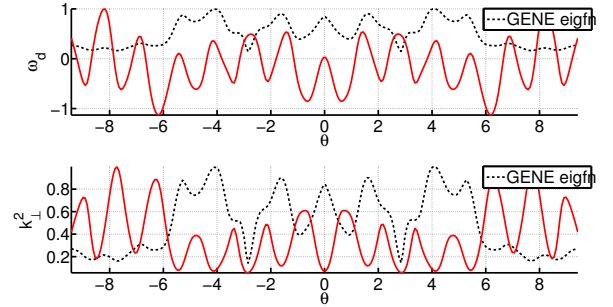


FIG. 14. Linear eigenfunction for case sa1, compared to un-averaged, unitary normalized drift and FLR coefficients.

difference in the magnitude of the growth rates, to within approximately ten percent. (This occurs in spite of the fact that the mode amplitudes *are* often finite within these extended domains.)

We show an example of the extended eigenfunction for case sa1 in a domain length of three full poloidal circuits in Figure 14, plotted separately against the unit normalized $\hat{\omega}_d$ and \hat{k}_\perp^2 coefficients. It can clearly be seen how the peaks and troughs in the eigenfunction amplitude correspond to the troughs and peaks of $\hat{\omega}_d$ and \hat{k}_\perp^2 – neither one is sufficient by itself to explain the distribution. This behavior is clearly apparent throughout the eigenfunction results.

One may ask the question of what happens when the width of the mode is increased or decreased in the an-

alytic model, e.g., do the growth rates converge in that model, similarly to how they converge in GENE? In some cases, this is observed. The reason this occurs is that the analytic spectra eventually shift to such large wavelengths (small b), due to strong \hat{k}_\perp^2 damping at larger b (as the polarization coefficient is always multiplied by b), that the polarization effect is sufficiently diminished to balance the drive. (This naturally only occurs for cases with small \hat{s} , $\hat{s} < 1$; since \hat{k}_\perp^2 scales with \hat{s}^2 , when $\hat{s} > 1$ then the stabilizing magnitude of \hat{k}_\perp^2 will increase quadratically with the increase in the mode width, whereas the drift coefficient $|\hat{\omega}_d|$ only scales linearly with \hat{s} (through its dependence on Λ) and hence does not overcome this effect.) Overall this suggests the rule of thumb that systems with $\hat{s} \gg 1$ will have ITG modes typically

confined in one poloidal circuit width.

What happens when the analytic gaussian width is decreased from one poloidal circuit length is that the most unstable mode is the one with the smallest width, centered *only* in the curvature wells where $\hat{\omega}_d$ is most negative (i.e., the most unstable mode is a delta function). This type of mode is never seen in the numerical results; presumably the kinetic effects overwhelmingly force the mode to be extended. In fact, this appears a plausible explanation for the enhanced stabilization of cases t3 and t4, which have such a short well in the polarization (t3) and curvature *and* polarization terms (t4) as to plausibly induce kinetic stabilization effects.

E. Principles of geometry optimization

We have shown that the analytic estimates for the growth rates provide reasonable agreement with the numerical solutions; thus we are able to outline, based on the analytic models and results, the general principles involved in improving the geometries. It is clear from inspection of equation 14 that the growth rate scales roughly with the geometry factors as $\gamma \sim |\langle \hat{\omega}_d \rangle^{-\text{sign}(\hat{\omega}_d)} / \langle \hat{k}_\perp^2 \rangle|^{0.5}$ (where $\text{sign}(x) = 1$ when $x > 0$, $\text{sign}(x) = -1$ when $x < 0$). Thus a rough form of the proxy function for the growth rate may be defined as $\chi = |\langle \hat{\omega}_d \rangle^{-\text{sign}(\hat{\omega}_d)} / \langle \hat{k}_\perp^2 \rangle|^{0.5}$. There are essentially three distinct mechanisms for minimization of χ . Referring to equations 40, 41 and ignoring the pressure term and constant normalization factors, these are minimization of $\langle \kappa_n / |\nabla\psi| \rangle$, $\langle -\Lambda \kappa_g / |\nabla\psi| \rangle$, and maximization of $\langle (1 + \Lambda^2) / |\nabla\psi|^2 \rangle$. Optimization of the first two targets is equivalent to the ‘ K_1 boosting’ discussed in⁹. The first mechanism represents curvature drive minimization, the second similarly but with a different physical manifestation, and the third the shear, FLR, polarization effects. The reason why these effects are distinct is because control of one does not necessarily have any bearing on control of another. For example, keeping the major radius R fixed, but taking the aspect ratio $\epsilon = \rho/R \rightarrow 0$, $\iota \rightarrow 0$, then $\kappa_n \rightarrow -1/R$ while $\kappa_g \rightarrow 0$. In other words, the normal and geodesic curvatures are bounded independently of one another. Similarly, consider a helical curve on a cylinder. Then, in the limit $\iota \rightarrow \infty$, $\kappa_n \rightarrow -1/\rho$, while $\tau_n \rightarrow \infty$, and recall that $\Lambda \sim \int (2\tau_n - \sigma)$.

Since the instability mechanisms are distinct they necessitate distinctive consideration; in what follows, we discuss each of the relevant factors in turn. First we mention that the general surface parameters of the transform ι and global shear \hat{s} have been shown to play an important role. The transform plays a strong generic control on κ_n , whereas the magnitude of \hat{s} correlates strongly with Λ and hence the polarization stabilization. The $|\nabla\psi|$ term is another evident way in which the the curvature and polarization terms may be controlled. It acts as an envelope factor, making the curvature worse as it is reduced, but the polarization better. It is particularly important

for the polarization term, as can be seen from Figure 10, case si2b, where \hat{k}_\perp^2 is large even where $\Lambda \sim 0$, which can only be due to the envelope effect of the surface proximity factor.

Next we make some general remarks concerning the bad curvature drive. 3-D shaping may reduce the connection length for $\kappa_n L$ more than 2-D shaping; in 2-D, the connection length depends on the fixed outboard surface area, whereas in 3-D, the rotation or deformation of the surface may actually reduce the outboard surface area over which the field line must pass. Nevertheless, the presence of bad (negative) normal curvature cannot generally be eliminated. Furthermore its gross magnitude scales similarly in 3-D as in 2-D. For this reason, we focus the remaining discussion on the other mechanisms.

Maximization of \hat{k}_\perp^2 is related to maximization of torsion and hence local and global shear. Roughly speaking, the more shaping a system has, the larger will be the torsion, since the poloidal field tends to be strong near prolate features or cusps. However, the torsion is also bounded by the level of global shear. To understand this, we revisit equation 38. First we introduce the definitions of the MHD shear and pressure parameters, $\hat{s} = -B_0 \rho^2 \iota' / \iota$ and $\hat{\alpha} = \frac{-2\mu_0 \rho^2 \nu'}{\iota^2 B_0}$. Using these parameters equation 38 may be rewritten

$$-\hat{s} \left(\frac{4\pi^2}{V'} \right) \frac{\iota}{\psi_0} = \sigma \left\langle \frac{B^2}{g^{\psi\psi}} \right\rangle - \hat{\alpha} \left\langle \frac{B^2}{g^{\psi\psi}} \lambda \right\rangle \frac{\iota^2 B_0^2}{2\mu_0 \psi_0} - 2 \left\langle \frac{B^2}{g^{\psi\psi}} \tau_n \right\rangle \quad (42)$$

where $\psi_0 = B_0 \rho^2$ is used. At fixed ι and the low beta $\hat{\alpha} \ll 1$ limit, equation 42 becomes a linear relationship between the shear parameter \hat{s} , the ‘averaged torsion’ due to field shaping $\bar{\tau}_n$, and the net parallel currents σ ,

$$\sigma = -\nu \hat{s} + 2\bar{\tau}_n \quad (43)$$

where $\nu = 4\pi^2 \iota / (V' \psi_0) / \langle B^2 / g^{\psi\psi} \rangle > 0$ and $\bar{\tau}_n = \langle B^2 \tau_n / g^{\psi\psi} \rangle / \langle B^2 / g^{\psi\psi} \rangle$. The coefficient $\bar{\tau}_n$ reflects the strong correlation between surface shape or torsion and surface current, and thereby via Λ to instability effects, as discussed in³³ and references therein. Equation 43 clearly shows how the torsion is constrained by the magnitude of the global shear. The proxy suggests that an optimal shaping should maximize the ratio of the torsion (or more precisely, Λ) to the bad curvature.

In tokamaks the torsion tends to be everywhere single signed, and the magnitude of $\bar{\tau}_n$ (or σ) has considerable manipulability due to shaping; in 3-D, the torsion changes sign depending on the local position on the surface. A plot of the non-dimensionalized averaged torsion versus net currents is shown for the 2-D cases (t0, t1, etc.) in Figure 15. Though they all have the same transform and global shear, the shaping changes have a substantial effect on the quantity $\bar{\tau}_n$. The reason why cases t3 and t4 have so much higher net torsion is because the poloidal shaping induces extremely large local torsion at the tapered points at the roughly $\pm\pi/2$ locations. This effect is much stronger for t4 than t3 because the tips are located on the inboard, at smaller radius of curvature. The very large torsion and current is what makes

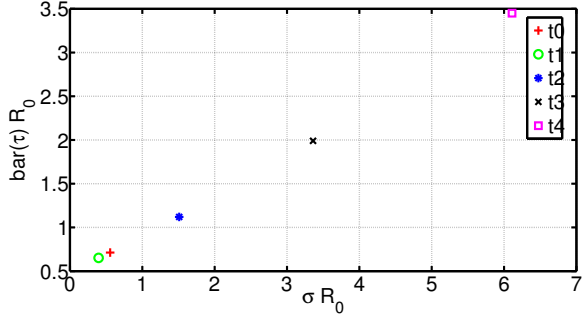


FIG. 15. Comparison of non-dimensionalized net torsion versus net currents.

the local shear undertake much greater variations than the other 2-D cases, even at fixed global shear, in turn making \hat{k}_\perp^2 much larger and enhancing stability.

Finally, we consider the $-\Lambda\kappa_g$ mechanism. Making use of equation 43 in 35, we can write the integrated local shear – geodesic curvature term as

$$-\Lambda\kappa_g = -\nu\kappa_g\hat{s}\frac{g^{\psi\psi}}{B}\int_{\eta_k}^{\eta}d\eta\sqrt{g}\frac{B^2}{g^{\psi\psi}} + 2\kappa_g\frac{g^{\psi\psi}}{B}\int_{\eta_k}^{\eta}d\eta\sqrt{g}\frac{B^2}{g^{\psi\psi}}(\bar{\tau}_n - \tau_n). \quad (44)$$

for tokamaks or systems with net currents. This relation frequently aids interpretation of the $-\Lambda\kappa_g$ behavior in the field line geometry plots for the 2-D cases. In systems where the net currents are negligible, as in the 3-D cases presented here, we can simply write

$$-\Lambda\kappa_g = -2\kappa_g\frac{g^{\psi\psi}}{B}\int_{\eta_k}^{\eta}d\eta\sqrt{g}\frac{B^2}{g^{\psi\psi}}\tau_n. \quad (45)$$

Thus, attaining stabilization of this term in 3-D is closely related to the simple condition $\kappa_g \cdot \tau_n < 0$ for $\eta > 0$ (and vice versa for $\eta < 0$). The sign dependence may be physically interpreted. When $\tau_n > 0$, the field line twists clockwise (facing along the field) around the surface. When $\kappa_g > 0$, the field line leads the surface geodesics behind it. When the field line simultaneously leads the surface while twisting into it, it is in a continuum buckling state, which yields a destabilizing Rayleigh-Taylor contribution. In contrast, a stabilizing effect occurs when the torsion opposes the geodesic curvature, and the field line is in a state of tautening. A similar interpretation can be made for the first term of 44, representing the global shear effect which goes as $-\kappa_g \cdot \hat{s}$. This term is destabilizing when the field lines lead ahead of the surface, but are radially sheared in the opposite direction.

The results of cases t3 and t4 show the geodesic-shear ($-\lambda\kappa_g$ term) can be made to dominate the normal curvature. It has also been noted that the geodesic-shear term is related to beneficial effects of negative shear in tokamaks (see e.g. reference²³). Insofar as 3-D geometry has a potential to have a locally stabilizing effect, inde-

pendent of global factors such as ι or \hat{s} , the curvature-shear term may be an important control. Thus this effect compels detailed consideration as a potential tool for optimization.

In attempting to understand optimization of the $-\Lambda\kappa_g$ term, a few concepts naturally arise and prove useful. Firstly, this is the concept of the *polarities* of the curvatures, i.e., their sign along the field line away from a particular point (e.g., κ_g going $-/+$ about $\eta = 0$ on the outboard midplane of a circular torus), as this determines what sign the torsion should take to make $-\Lambda\kappa_g$ stabilizing – or vice versa. Similarly, it is necessary or at least helpful to understand the concept of the *symmetries* of the curvatures, i.e., in what regions of the surface they take what sign, depending on the geometry. This determines how long or to what extent the term will remain stabilizing.

In what follows we outline how these concepts may be qualitatively and semi-quantitatively understood. Firstly, this is via relation to the generalized toroidal ‘edges’ of the surface. The generalized edges can be defined as the locations where either one or both of the surface distance functions, $R(\theta, \zeta)$, $Z(\theta, \zeta)$, take their extremal values. These are the locations of interest for the instability studies, as they include the points of worst normal curvature. The polarity changes are often centered about the edges. Some simplified analysis about the edge points may be accomplished via Taylor expansion of the curvature formulas. For example, expanding about the point (θ_0, ζ_0) where R and Z are extremal, i.e. $R_\theta = 0, R_\zeta = 0$, and similarly for Z , and denoting the function values at these points with a hat, i.e. $\hat{R} = R(\theta_0, \zeta_0)$, we can Taylor expand the normal curvature to find the relatively simple relation

$$\begin{aligned} \kappa_n = & \frac{1}{AL^2} \times [\hat{R}\hat{Z}_\theta w \\ & + \Delta\theta\Delta\zeta(\hat{R}_{\theta\zeta}\hat{Z}_\theta(w - 4\hat{R}_{\zeta\zeta}) + 2(\hat{Z}_\zeta - \iota\hat{Z}_\theta)(\hat{R}_{\zeta\zeta}\hat{R}_{\theta\theta} + \hat{R}_{\theta\zeta}^2)) \\ & + (\Delta\theta)^2(\frac{1}{2}\hat{R}_{\theta\theta}\hat{Z}_\theta w + 2(\hat{R}_{\theta\theta}\hat{Z}_\zeta - \hat{R}_{\theta\zeta}\hat{Z}_\theta)(\hat{R}_{\theta\zeta} + \iota\hat{R}_{\theta\theta})) \\ & + (\Delta\zeta)^2(\frac{1}{2}\hat{R}_{\zeta\zeta}\hat{Z}_\theta w + 2(\hat{R}_{\theta\zeta}\hat{Z}_\zeta - \hat{R}_{\zeta\zeta}\hat{Z}_\theta)(\hat{R}_{\zeta\zeta} + \iota\hat{R}_{\theta\zeta})] \end{aligned} \quad (46)$$

where the parameters A and L are those given above, and $w = -\hat{R} + \hat{R}_{\zeta\zeta} + 2\iota\hat{R}_{\theta\zeta} + \iota^2\hat{R}_{\theta\theta}$. Note that the $\Delta\theta = \theta - \theta_0$, $\Delta\zeta = \zeta - \zeta_0$ terms vanish at \mathbf{x}_0 .

The symmetries may be understood by aid of considering the curvature null lines, the (independent) lines where $\kappa_n = 0, \kappa_g = 0, \tau_n = 0$. The curvatures flip when a field line crosses a curvature null line (by definition), and the intersections of the null lines therefore determine the curvature symmetries or symmetry regions. In a 2-D system, the edges and null lines are toroidally fixed, so that the symmetry regions can be deduced from inspection of a single cross section. In 3-D systems, the situation is complicated by the fact that the cross section may either translate, rotate, or deform. If the cross section merely rotates, then the edges simply rotate with the cross section; thus the null lines mostly simply rotate. In the case

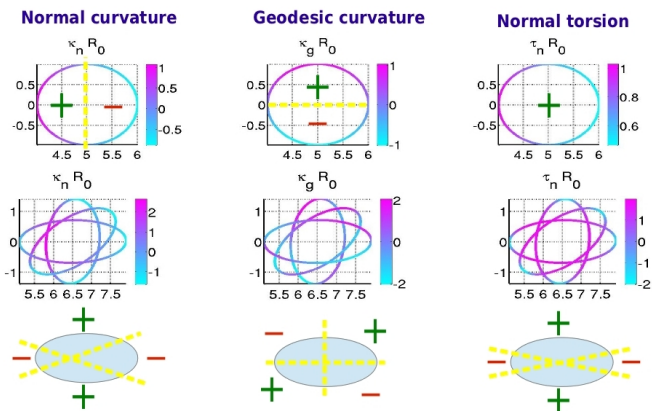


FIG. 16. Cross sections of a canonical 2-D case, a circular tokamak (first row), and a canonical 3-D case, a purely rotating cross section (second row), with normal curvature, geodesic curvature, and torsion shown in the columns, respectively. The direction to the outboard is towards the right. The curvature null lines are highlighted in yellow, and the positive and minus signs emphasize the symmetry distributions between them. The field points out of the page, and the net direction of surface and field line rotation is counterclockwise.

of deformation, what happens is that the edges both vanish and reform as one moves in the toroidal direction; the null line behavior is therefore more complicated as well.

To illustrate an example of the symmetry behaviors, a canonical 2-D and 3-D case are shown in Figure 16. There, it can be seen how the 2-D system has symmetry distributions which are predominantly left/right and up/down, whereas in 3-D, the symmetry distributions become dominated by the presence of the edges. (However, since $\iota \sim O(1)$ the normal curvature still tends to be biased negative on the outboard; thus a partially left/right distribution is retained.) Another key difference between the 2-D and 3-D systems is in the torsion, as in the tokamak, the current tends to drive the field all one way (i.e. counterclockwise in the Figure 16) around the poloidal cross section, whereas in 3-D, the torsion is geometrically negative on the prolate edges and positive on the oblate locations, albeit constrained to be zero or negative on average due to relation 43. Thus in a 3-D system, the sign of the torsion somewhat mimics the sign of the normal curvature. The null lines of the geodesic curvature tend to be $\pi/2$ out of phase with the normal curvature in a canonical 2-D system, whereas in a canonical 3-D system, the phase shift is decreased due to the presence of additional generalized edges; in the 3-D case of Figure 16 the phase shift is roughly $\pi/4$.

We may demonstrate the utility of this conceptual framework by making analysis of the curvature-shear behavior in three different, fundamental cases (see field line geometry plots above). Firstly, in the case of the simplistic 2-D system (e.g. case t0), with the field line starting from the outboard midplane, κ_g clearly has polarity $-/+$ about $\eta = 0$ and since τ_n is everywhere positive, the curvature-shear is destabilizing about the center of the

flux tube. For case t4 presented above, the key control is that the geodesic curvature polarity is flipped about $\theta \sim \pi/2$, stabilizing the overall term. In the 3-D case, starting from the outboard midplane at the prolate location (case si0), the geodesic curvature has a reversed polarity, $+/-$ about $\eta = 0$. This polarity change appears to be a general difference between 2-D and 3-D systems, at least under the approximations of these results ($\bar{\theta} = \theta$, etc.). The torsion is at first negative, then positive after roughly $\pi/4$ radians off of the edge, such that the curvature-shear is at first destabilizing. Lastly, in the 3-D case starting from the outboard midplane at the oblate location (case si0b), the κ_g polarity is $-/+$, and the torsion is positive, making the contribution destabilizing again. However, viewing the field line data for case si0 versus si0b, it is clear that the curvature-shear for case si0 is qualitatively superior than for the oblate position, si0b. This is evidently due to the fact that the null lines of the torsion are closely centered around the prolate edge, so that on the prolate location, $\kappa_g \cdot \tau_n$ has a shorter connection length than for the oblate location, as well as overall better phasing, which makes the contribution more stabilizing.

The point of these examples is that the curvature-shear contribution may be sensibly analyzed and in principle, the mutual phases of κ_g and τ_n (as well as e.g. $|\nabla\psi|$ and $B_p(\theta, \zeta)$ as necessary) should be open to optimization in a numerical scheme. Furthermore, the discussion sheds light on the utility of the deformation effect. This is because it is clear that a purely rotating geometry can only do so much to alter its distribution of curvatures, because the null lines and symmetries essentially merely rotate with the cross section (albeit with some typical persistence of an inboard/outboard normal curvature symmetry). However, in a case including deformation, as shown in the results, the symmetry (null) lines are not fixed to mere rotation, and thus the phases of the curvatures may be selectively tailored. The null lines may be forced to rotate faster than normal or even to counter-rotate from the usual direction, as e.g. case si2 in Figure 11, where the helical curvature component is clearly reduced. We note that these principles may be just as useful for understanding minimization of κ_n wells or optimization of the torsional distribution for \hat{k}_\perp^2 .

VI. CONCLUSIONS

In conclusion, we have investigated a modeling framework of analytic ITG theory, numerical computation, and local 3-D equilibrium theory for understanding minimization of maximum linear growth rates of ITG modes in toroidal geometries. The analytic model for the growth rate is given in equation 14, scaling roughly as $\chi = |\langle \hat{\omega}_d \rangle^{-\text{sign}(\hat{\omega}_d)} / \langle \hat{k}_\perp^2 \rangle|^{0.5}$. The analytic growth rate gives reasonable agreement in trend with the comparable results from numerical solution over a wide range of 2-D and 3-D geometric cases.

The geometric cases explore differences in shaping principally due to the alteration of concavity, and in 3-D, the differences between cross sectional rotation and deformation. One case (t0) also employs a modified field strength distribution, whereas all other cases use the simplistic straight field line coordinate assumption $\bar{\theta} = \theta$. The geometries are analyzed using field line geometric plots, 2-D cross sectional plots, 3-D surface plots, and 2-D surface plots. Certain geometries are stabilized by enhancement of the FLR coefficient (such as case t3), whereas others are stabilized via both drastic positive biasing of $\hat{\omega}_d$ via the integrated local shear - geodesic curvature term *and* boosting of the FLR coefficient (such as case t4). The stellarator cases studied show improvements within their sequences primarily due to increased global shear (higher net torsion) and improved behaviors in the FLR and/or curvature-shear term. The outboard midplane prolate location appears generally more stable than the oblate location.

While it seems clear that in general, bad normal curvature may be reduced via 3-D shaping, the complementary effects of the shear-curvature and FLR terms are arguably the tools of most interest, as the presence of bad normal curvature cannot generally be eliminated. Improvements to the curvature-shear term relies on manipulation of the curvature polarities and symmetries. These in turn may be fruitfully characterized using the notions of the surface edges and curvature null lines. These conceptual tools greatly facilitate understanding how the shape of an arbitrary surface relates to its overall geometric and instability properties; they should prove useful for guidance and analysis of numerical optimization results.

There are a few most important ways in which the present results might be extended or applied. Firstly, the results would benefit from a closer comparison or mutual understanding with neoclassical optimization targets, not considered in the present study. These targets also depend crucially on the curvatures (and global B field distribution) and hence the curvature coefficients. Secondly, the results could be extended by making a further effort to elucidate the possible optimization over kinetic ITG effects, which are not considered here. Thirdly, the important metrics from the present study (e.g. the averaged normal curvature, geodesic-shear, the FLR term; their symmetries, magnitudes, and distributions) could be used to make a more targeted classification of the general shaping space explored in numerical optimization routines.

VII. ACKNOWLEDGEMENTS

This report is an extended version of a corresponding paper done in collaboration with Chris Hegna, Harry Mynick, Pavlos Xanthopoulos, and M. J. Pueschel. This work was supported by U.S. DoE grant numbers DE-FG02-99ER54546 and DE-SC0006103. We gratefully ac-

knowledge the support and discussion of T. Bird, J. D. Callen, M. Landreman, T. Rafiq, P. Terry, the HSX laboratory members and the CPTC faculty, students, and staff. We also thank C. Sovinec for providing a computing allocation with the National Energy Research Scientific Computing Center.

VIII. APPENDIX: SHAPING PARAMETRIZATIONS

In this appendix we list the shaping parametrizations used in the results; first we give the parametrizations, and then the specific parameters used. Selection of parametrizations was heuristic and guided by inspection of toroidal cross sectional slices during construction. Care was taken to avoid unrealistic features, such as sharp edges or cusps, which might be expected to generate large electric fields similar to ordinary conducting surfaces¹⁰². For more intricate 3-D shaping the $(0, n)$ harmonic (axial translation) was often found to be important for maintaining a convergent equilibrium solution, though its overall affect on the shaping is slight.

1. t0, t1

$$\begin{aligned} R &= R_0 + \rho \cos \bar{\theta} \\ Z &= \rho \sin \bar{\theta}. \end{aligned}$$

$$\{R_0, \rho, V'\} = \{5, 1, 1\}$$

2. t2

$$\begin{aligned} R &= R_0 + \rho_d \cos(\bar{\theta} + \kappa \sin \bar{\theta}) \\ Z &= \rho_Z \sin \bar{\theta}. \end{aligned}$$

$$\{R_0, \rho_d, \kappa, \rho_Z, V'\} = \{5, 1, .51, 2.2\rho_d, 1\}$$

3. t3, t4

$$\begin{aligned} R &= R_0 + \rho_R(\rho_3 \cos \bar{\theta} + s \cosh(\rho_4 \sin \bar{\theta}/\rho_R)) \\ Z &= d\rho_Z \sin \bar{\theta}. \end{aligned}$$

$$\text{t3: } \{R_0, \rho_R, \rho_3, s, \rho_4, \rho_Z, V'\} = \{4.4, 0.6, 1, 1, 1, 1.5, 1\}$$

$$\text{t4: } \{\cdot, s\} = \{\cdot, -1\}$$

4. sa0, sa1, sa2, sa3

$$\begin{aligned} R &= R_0 + \rho_0 \cos \bar{\theta} - \rho_2 \cos(\bar{\theta} - N\bar{\zeta}) - \rho_3 \cos(2\bar{\theta} - N_2\bar{\zeta}) \\ Z &= R_0 + \rho_0 \sin \bar{\theta} + \rho_2 \sin(\bar{\theta} - N\bar{\zeta}) + \rho_3 \sin(2\bar{\theta} - N_2\bar{\zeta}). \end{aligned}$$

$$\text{sa0: } \{R_0, \rho_0, \rho_2, N, \rho_3, N_2, V'\} = \{6.5, 1.05, \rho_0/3, 6, \rho_2/10, 9, 1\}$$

$$\text{sa1: } \{\cdot, \rho_3\} = \{\cdot, 0\}$$

$$\text{sa2: } \{\cdot, \rho_3\} = \{\cdot, -\rho_2/10\}$$

$$\text{sa3: } \{\cdot, \rho_3\} = \{\cdot, -2\rho_2/10\}$$

5. si0, si1, si2

$$\begin{aligned}
R &= R_0 + \rho_0 \cos \bar{\theta} (1 + \rho_6 \cos(N_4(\bar{\zeta} - o_1))^2) \\
&\quad + \rho_2 \cos(\bar{\theta} - N(\zeta - o_1))(1 - \rho_4 \sin(N_4(\zeta - o_1))^2) \\
&\quad + \rho_3 \cos(2\bar{\theta} - N_2(\bar{\zeta} - o_1) - o_2) \sin(N/2(\bar{\zeta} - o_1)) \\
&\quad + \rho_5 \cos(M\bar{\theta} - N_3(\bar{\zeta} - o_1)) \sin(N/2(\bar{\zeta} - o_1))^2 \\
&\quad + \delta \cos(N(\bar{\zeta} - o_1)) \\
Z &= \rho_0 \sin \bar{\theta} (1 + \rho_6 \cos(N_4(\bar{\zeta} - o_1))^2) \\
&\quad - \rho_2 \sin(\bar{\theta} - N(\zeta - o_1))(1 - \rho_4 \sin(N_4(\zeta - o_1))^2) \\
&\quad - \rho_3 \sin(2\bar{\theta} - N_2(\bar{\zeta} - o_1) - o_2) \sin(N/2(\bar{\zeta} - o_1)) \\
&\quad - \rho_5 \sin(M\bar{\theta} - N_3(\bar{\zeta} - o_1)) \sin(N/2(\bar{\zeta} - o_1))^2 \\
&\quad + \delta \sin(N(\bar{\zeta} - o_1))
\end{aligned}$$

Note: putting o_1 as $\pi/N, 0$ controls whether $\eta = 0$ lies at the oblate outboard midplane point or prolate outboard point; the parameter o_2 has a similar control with parameters $0, \pi/2$.

$$\begin{aligned}
\text{si0: } &\{R_0, \rho_0, \rho_6, N_4, \rho_2, N, \rho_4, \rho_3, N_2, \rho_5, M, N_3, \delta, V'\} \\
&= \{6.5, 1.05, 0, .5N, .4\rho_0, 5, 0, 0, 1.5N, 0, 3, 2N, 0, 1\} \\
\text{si1: } &\{\cdot, \rho_4, \rho_3, \rho_5\} = \{\cdot, .15, .225\rho_2, -.2\rho_3\} \\
\text{si2: } &\{\cdot, \rho_4, \rho_3, \rho_5, \rho_6, \delta\} = \\
&\{\cdot, 0, .5\rho_2, -.2\rho_3, -.2, .2\rho_0\}
\end{aligned}$$

- ¹A. H. Boozer, "Physics of magnetically confined plasmas," *Rev. Mod. Phys.* **76**, 1071–1141 (2005).
- ²A. H. Boozer, "Use of nonaxisymmetric shaping in magnetic fusion," *Physics of Plasmas* **16**, 058102 (2009).
- ³H. Wobig, "Theory of advanced stellarators," *Plasma Physics and Controlled Fusion* **41**, A159 (1999).
- ⁴H. E. Mynick, "Transport optimization in stellarators," *Physics of Plasmas* **13**, 058102 (2006).
- ⁵P. Helander, C. D. Beidler, T. M. Bird, M. Drevlak, Y. Feng, R. Hatzky, F. Jenko, R. Kleiber, J. H. E. Proll, Y. Turkin, and P. Xanthopoulos, "Stellarator and tokamak plasmas: a comparison," *Plasma Physics and Controlled Fusion* **54**, 124009 (2012).
- ⁶J. M. Canik, D. T. Anderson, F. S. B. Anderson, C. Clark, K. M. Likin, J. N. Talmadge, and K. Zhai, "Reduced particle and heat transport with quasisymmetry in the helically symmetric experiment," *Physics of Plasmas* **14**, 056107 (2007).
- ⁷H. E. Mynick, P. Xanthopoulos, and A. H. Boozer, "Geometry dependence of stellarator turbulence," *Physics of Plasmas* **16**, 110702 (2009).
- ⁸H. E. Mynick, N. Pomphrey, and P. Xanthopoulos, "Optimizing stellarators for turbulent transport," *Phys. Rev. Lett.* **105**, 095004 (2010).
- ⁹H. E. Mynick, N. Pomphrey, and P. Xanthopoulos, "Reducing turbulent transport in toroidal configurations via shaping," *Physics of Plasmas* **18**, 056101 (2011).
- ¹⁰H. Mynick, N. Pomphrey, P. Xanthopoulos, and M. Lucia, "Turbulent optimization in stellarators & tokamaks via shaping," in *Proceedings of the 24th IAEA Fusion Energy Conference* (IAEA, 2012) pp. TH-P2/04.
- ¹¹A. Fujisawa, "A review of zonal flow experiments," *Nuclear Fusion* **49**, 013001 (2009).
- ¹²W. Tang, "Microinstability theory in tokamaks," *Nuclear Fusion* **18**, 1089 (1978).
- ¹³W. Horton, "Drift waves and transport," *Rev. Mod. Phys.* **71**, 735–778 (1999).
- ¹⁴J. Weiland, *Collective modes in inhomogeneous plasma: kinetic and advanced fluid theory* (Taylor & Francis, 2000).
- ¹⁵D. Swanson, *Plasma Waves*, Series in Plasma Physics (Institute of Physics Pub., 2003).
- ¹⁶P. Diamond, S. Itoh, and K. Itoh, *Modern Plasma Physics*, Modern Plasma Physics (Cambridge University Press, 2008).
- ¹⁷P. W. Terry, "Suppression of turbulence and transport by sheared flow," *Rev. Mod. Phys.* **72**, 109–165 (2000).
- ¹⁸D. Spong, J. Harris, A. Ware, S. Hirshman, and L. Berry, "Shear flow generation in stellaratorsconfigurational variations," *Nuclear Fusion* **47**, 626 (2007).
- ¹⁹P. Xanthopoulos, A. Mischchenko, P. Helander, H. Sugama, and T.-H. Watanabe, "Zonal flow dynamics and control of turbulent transport in stellarators," *Phys. Rev. Lett.* **107**, 245002 (2011).
- ²⁰J. H. E. Proll, P. Helander, J. W. Connor, and G. G. Plunk, "Resilience of quasi-isodynamic stellarators against trapped-particle instabilities," *Phys. Rev. Lett.* **108**, 245002 (2012).
- ²¹F. Jenko, W. Dorland, M. Kotschenreuther, and B. N. Rogers, "Electron temperature gradient driven turbulence," *Physics of Plasmas* **7**, 1904–1910 (2000).
- ²²F. Romanelli, "Ion temperature-gradient-driven modes and anomalous ion transport in tokamaks," *Physics of Fluids B: Plasma Physics* **1**, 1018–1025 (1989).
- ²³S. Guo and J. Weiland, "Analysis of eta(i) mode by reactive and dissipative descriptions and the effects of magnetic q and negative shear on the transport," *Nuclear Fusion* **37**, 1095–1107 (1997).
- ²⁴C. C. Hegna, "Local three-dimensional magnetostatic equilibria," *Physics of Plasmas* **7**, 3921–3928 (2000).
- ²⁵J. L. V. Lewandowski, "Gyrokinetic simulations of microinstabilities in stellarator geometry," *Physics of Plasmas* **10**, 4053–4063 (2003).
- ²⁶M. N. Rorvig, Master's thesis, University of Wisconsin (2014).
- ²⁷S. C. Cowley, R. M. Kulsrud, and R. Sudan, "Considerations of ion-temperature-gradient-driven turbulence," *Physics of Fluids*

- B: Plasma Physics **3**, 2767–2782 (1991).
- 28 J. Anderson, T. Rafiq, M. Nadeem, and M. Persson, “A comparison of drift wave stability in stellarator and tokamak geometry,” *Physics of Plasmas* **9**, 1629–1636 (2002).
 - 29 X. Garbet, “Turbulence in fusion plasmas: key issues and impact on transport modelling,” *Plasma Physics and Controlled Fusion* **43**, A251 (2001).
 - 30 A. H. Boozer, “Control of non-axisymmetric toroidal plasmas,” *Plasma Physics and Controlled Fusion* **52**, 104001 (2010).
 - 31 J. Anderson, H. Nordman, and J. Weiland, “Effects of non-circular tokamak geometry on ion-temperature-gradient driven modes,” *Plasma Physics and Controlled Fusion* **42**, 545 (2000).
 - 32 P. Angelino, X. Garbet, L. Villard, A. Bottino, S. Jolliet, P. Ghendrih, V. Grandgirard, B. F. McMillan, Y. Sarazin, G. Dif-Pradalier, and T. M. Tran, “Role of plasma elongation on turbulent transport in magnetically confined plasmas,” *Phys. Rev. Lett.* **102**, 195002 (2009).
 - 33 E. A. Belli, G. W. Hammett, and W. Dorland, “Effects of plasma shaping on nonlinear gyrokinetic turbulence,” *Physics of Plasmas* **15**, 092303 (2008).
 - 34 Z. Gao, L. Peng, P. Wang, J. Dong, and H. Sanuki, “Plasma elongation effects on temperature gradient driven instabilities and geodesic acoustic modes,” *Nuclear Fusion* **49**, 045014 (2009).
 - 35 N. Joiner and W. Dorland, “Ion temperature gradient driven transport in tokamaks with square shaping,” *Physics of Plasmas* **17**, 062306 (2010).
 - 36 A. Kendl, “Local shear damping of ion and electron temperature gradient modes,” *Physics of Plasmas* **11**, 1810–1815 (2004).
 - 37 A. Kendl and B. D. Scott, “Flux-surface shaping effects on tokamak edge turbulence and flows,” *Physics of Plasmas* **13**, 012504 (2006).
 - 38 A. KENDL, “Plasma turbulence in complex magnetic field structures,” *Journal of Plasma Physics* **72**, 1145–1148.
 - 39 J. E. Kinsey, R. E. Waltz, and J. Candy, “The effect of plasma shaping on turbulent transport and $e \times b$ shear quenching in nonlinear gyrokinetic simulations,” *Physics of Plasmas* **14**, 102306 (2007).
 - 40 X. Lapillonne, *Local and global Eulerian gyrokinetic simulations of microturbulence in realistic geometry with applications to the TCX Tokamak*, Ph.D. thesis (2009).
 - 41 M. A. Mahmood, T. Rafiq, and M. Persson, “Unstable ion-temperature-gradient modes in an advanced tokamak plasma,” *Plasma Physics and Controlled Fusion* **48**, 1019 (2006).
 - 42 R. L. Miller, M. S. Chu, J. M. Greene, Y. R. Lin-Liu, and R. E. Waltz, “Noncircular, finite aspect ratio, local equilibrium model,” *Physics of Plasmas* **5**, 973–978 (1998).
 - 43 Y.-K. M. Peng, “The physics of spherical torus plasmas,” *Physics of Plasmas* **7**, 1681–1692 (2000).
 - 44 E. J. Strait, “Stability of high beta tokamak plasmas@f—,” *Physics of Plasmas* **1**, 1415–1431 (1994).
 - 45 R. E. Waltz and R. L. Miller, “Ion temperature gradient turbulence simulations and plasma flux surface shape,” *Physics of Plasmas* **6**, 4265–4271 (1999).
 - 46 A. Bhattacharjee, J. E. Sedlak, P. L. Similon, M. N. Rosenbluth, and D. W. Ross, “Drift waves in a straight stellarator,” *Physics of Fluids* **26**, 880–882 (1983).
 - 47 N. Dominguez, B. A. Carreras, V. E. Lynch, and P. H. Diamond, “Dissipative trapped electron modes in $l=2$ torsatrons,” *Physics of Fluids B: Plasma Physics* **4**, 2894–2906 (1992).
 - 48 A. Kendl and H. Wobig, “Geometric effects on drift wave stability in advanced stellarators,” *Physics of Plasmas* **6**, 4714–4721 (1999).
 - 49 R. Kleiber, “Resistive drift modes in general geometry,” *Physics of Plasmas* **8**, 4090–4095 (2001).
 - 50 J. L. Lewandowski, “A simple model for collisional drift waves,” *Canadian Journal of Physics* **75**, 891–906 (1997), <http://www.nrcresearchpress.com/doi/pdf/10.1139/p97-038>.
 - 51 J. L. V. Lewandowski and R. M. Ellem, “Effect of radial wavevector on collisional drift waves in a toroidal heliac,” *Australian Journal of Physics* **52**, 71–85 (1999).
 - 52 J. L. Lewandowski, “Collisional drift waves in stellarator plasmas,” *Canadian Journal of Physics* **81**, 1309–1330 (2003), <http://www.nrcresearchpress.com/doi/pdf/10.1139/p03-108>.
 - 53 M. Nadeem, T. Rafiq, and M. Persson, “Local magnetic shear and drift waves in stellarators,” *Physics of Plasmas* **8**, 4375–4385 (2001).
 - 54 M. H. Nasim, T. Rafiq, and M. Persson, “Geometrical effects on drift wave stability in low shear stellarator plasmas,” *Plasma Physics and Controlled Fusion* **46**, 193 (2004).
 - 55 M. Persson, J. L. V. Lewandowski, and H. Nordman, “Drift waves in helical symmetry,” *Physics of Plasmas* **3**, 3720–3724 (1996).
 - 56 M. Persson and J. L. V. Lewandowski, “Localization of drift waves in a helically symmetric stellarator model,” *Plasma Physics and Controlled Fusion* **39**, 1941 (1997).
 - 57 M. Persson, M. Nadeem, J. L. V. Lewandowski, and H. J. Gardner, “Drift waves in stellarator geometry,” *Plasma Physics and Controlled Fusion* **42**, 203 (1999).
 - 58 T. Rafiq and C. C. Hegna, “Drift waves in helically symmetric stellarators,” *Physics of Plasmas* **12**, 112505 (2005).
 - 59 G. Rewoldt, L.-P. Ku, and W. M. Tang, “Comparison of microinstability properties for stellarator magnetic geometries,” *Physics of Plasmas* **12**, 102512 (2005).
 - 60 P. Uddholm, M. Nadeem, and M. Persson, “Approximate localization and dispersion curves of drift waves in straight stellarators,” *Plasma Physics and Controlled Fusion* **42**, 501 (2000).
 - 61 R. E. Waltz and A. H. Boozer, “Local shear in general magnetic stellarator geometry,” *Physics of Fluids B: Plasma Physics* **5**, 2201–2205 (1993).
 - 62 T. M. Bird and C. C. Hegna, “A model for microinstability destabilization and enhanced transport in the presence of shielded 3d magnetic perturbations,” *Nuclear Fusion* **53**, 013004 (2013).
 - 63 P. Cuthbert, J. L. V. Lewandowski, H. J. Gardner, M. Persson, D. B. Singleton, R. L. Dewar, N. Nakajima, and W. A. Cooper, “Toroidally localized and nonlocalized ballooning instabilities in a stellarator,” *Physics of Plasmas* **5**, 2921–2931 (1998).
 - 64 C. C. Hegna and S. R. Hudson, “Ideal magnetohydrodynamic ballooning stability boundaries in three-dimensional equilibria,” *Physics of Plasmas* **9**, 2014–2019 (2002).
 - 65 N. Nakajima, “High-mode-number ballooning modes in a heliotron/torsatron system. i. local magnetic shear,” *Physics of Plasmas* **3**, 4545–4555 (1996).
 - 66 J. B. Taylor, “Simple toroidal magnetic field with negative $v[\text{double-prime}]$,” *Physics of Fluids* **8**, 1203–1205 (1965).
 - 67 J. A. Baumgaertel, E. A. Belli, W. Dorland, W. Guttenfelder, G. W. Hammett, D. R. Mikkelsen, G. Rewoldt, W. M. Tang, and P. Xanthopoulos, “Simulating gyrokinetic microinstabilities in stellarator geometry with gs2,” *Physics of Plasmas* **18**, 122301 (2011).
 - 68 G. Jost, T. M. Tran, W. A. Cooper, L. Villard, and K. Appert, “Global linear gyrokinetic simulations in quasi-symmetric configurations,” *Physics of Plasmas* **8**, 3321–3333 (2001).
 - 69 V. Kornilov, R. Kleiber, R. Hatzky, L. Villard, and G. Jost, “Gyrokinetic global three-dimensional simulations of linear ion-temperature-gradient modes in wendelstein 7-x,” *Physics of Plasmas* **11**, 3196–3202 (2004).
 - 70 T. Kuroda, H. Sugama, R. Kanno, and M. Okamoto, “Ion temperature gradient modes in toroidal helical systems,” *Journal of the Physical Society of Japan* **69**, 2485–2492 (2000).
 - 71 M. NUNAMI, T.-H. WATANABE, and H. SUGAMA, “Gyrokinetic vlasov code including full three-dimensional geometry of experiments,” *Plasma and Fusion Research* **5**, 016–016 (2010).
 - 72 T. Rafiq, J. Anderson, M. Nadeem, and M. Persson, “Ion-temperature-gradient modes in stellarator geometry,” *Plasma Physics and Controlled Fusion* **43**, 1363 (2001).
 - 73 P. Xanthopoulos and F. Jenko, “Gyrokinetic analysis of linear microinstabilities for the stellarator wendelstein 7-x,” *Physics of Plasmas* **14**, 042501 (2007).

- ⁷⁴W. D'haeseleer, *Flux coordinates and magnetic field structure: a guide to a fundamental tool of plasma theory*, Springer series in computational physics (Springer-Verlag, 1991).
- ⁷⁵J. W. Connor, R. J. Hastie, and J. B. Taylor, "High mode number stability of an axisymmetric toroidal plasma," *Proceedings of the Royal Society A: Mathematical, Physical, and Engineering Sciences* **365**, 1–17 (1979).
- ⁷⁶R. Dewar, J. Manickam, R. Grimm, and M. Chance, "n-dependence of ballooning instabilities," *Nuclear Fusion* **21**, 493 (1981).
- ⁷⁷R. L. Dewar and A. H. Glasser, "Ballooning mode spectrum in general toroidal systems," *Physics of Fluids* **26**, 3038–3052 (1983).
- ⁷⁸J. Freidberg, *Ideal magnetohydrodynamics*, Modern perspectives in energy (Plenum Press, 1987).
- ⁷⁹W. A. Cooper, D. B. Singleton, and R. L. Dewar, "Spectrum of ballooning instabilities in a stellarator," *Physics of Plasmas* **3**, 275–280 (1996).
- ⁸⁰J. W. Connor, R. J. Hastie, and J. B. Taylor, "Stability of toroidal plasmas: the influence of magnetic shear, periodicity and rotation," *Plasma Physics and Controlled Fusion* **46**, B1 (2004).
- ⁸¹M. A. Beer, S. C. Cowley, and G. W. Hammett, "Field-aligned coordinates for nonlinear simulations of tokamak turbulence," *Physics of Plasmas* **2**, 2687–2700 (1995).
- ⁸²B. Scott, "Global consistency for thin flux tube treatments of toroidal geometry," *Physics of Plasmas* **5**, 2334–2339 (1998).
- ⁸³I. Pusztai, T. Fulop, J. Candy, and R. J. Hastie, "Collisional model of quasilinear transport driven by toroidal electrostatic ion temperature gradient modes," *Physics of Plasmas* **16**, 072305 (2009).
- ⁸⁴J. Weiland and A. Hirose, "Electromagnetic and kinetic effects on the ion temperature gradient mode," *Nuclear Fusion* **32**, 151 (1992).
- ⁸⁵R. Goldston and P. Rutherford, *Introduction to Plasma Physics*, Plasma Physics Series (Institute of Physics Pub., 1995).
- ⁸⁶P. Terry, W. Anderson, and W. Horton, "Kinetic effects on the toroidal ion pressure gradient drift mode," *Nuclear Fusion* **22**, 487 (1982).
- ⁸⁷A. H. Boozer, "Local equilibrium of nonrotating plasmas," *Physics of Plasmas* **9**, 3762–3766 (2002).
- ⁸⁸A. Skovoroda, "Geometric properties of plasma equilibrium near a given magnetic surface," *Plasma Physics Reports* **32**, 977–987 (2006).
- ⁸⁹A. A. Skovoroda, "Local geometrical properties of magnetic configurations with nested equilibrium magnetic surfaces," *Plasma Physics Reports* **35**, 269–272 (2009).
- ⁹⁰A. Skovoroda and I. Taimanov, "Role of the mean curvature in the geometry of magnetic confinement configurations," *Plasma Physics Reports* **36**, 819–823 (2010).
- ⁹¹B. O'Neill, *Elementary Differential Geometry, Revised 2nd Edition*, Elementary Differential Geometry Series (Elsevier Science, 2006).
- ⁹²A. Gray, E. Abbena, and S. Salamon, *Modern Differential Geometry of Curves And Surfaces With Mathematica*, Studies in Advanced Mathematics Series (Chapman & Hall CRC, 2006).
- ⁹³P. Helander and D. Sigmar, *Collisional Transport in Magnetized Plasmas*, Cambridge Monographs on Plasma Physics (Cambridge University Press, 2005).
- ⁹⁴K. Miyamoto, *Controlled Fusion and Plasma Physics*, Series in Plasma Physics (Taylor & Francis, 2006).
- ⁹⁵A. I. Morozov and L. S. Solov'ev, "The structure of magnetic fields," *Reviews of Plasma Physics* **2**, 1–100 (1966).
- ⁹⁶S. P. Hirshman, D. A. Spong, J. C. Whitson, B. Nelson, D. B. Batchelor, J. F. Lyon, R. Sanchez, A. Brooks, G. Y.-Fu, R. J. Goldston, L.-P. Ku, D. A. Monticello, H. Mynick, G. H. Neilson, N. Pomphrey, M. Redi, W. Reiersen, A. H. Reiman, J. Schmidt, R. White, M. C. Zarnstorff, J. W. H. Miner, P. M. Valanju, and A. Boozer, "Physics of compact stellarators," *Physics of Plasmas* **6**, 1858–1864 (1999).
- ⁹⁷S. P. Hirshman and J. C. Whitson, "Steepest-descent moment method for three-dimensional magnetohydrodynamic equilibria," *Physics of Fluids* **26**, 3553–3568 (1983).
- ⁹⁸X. Lapillonne, S. Brunner, T. Dannert, S. Jolliet, A. Marinoni, L. Villard, T. Gorler, F. Jenko, and F. Merz, "Clarifications to the limitations of the s-alpha equilibrium model for gyrokinetic computations of turbulence," *Physics of Plasmas* **16**, 032308 (2009).
- ⁹⁹T. Görler, *Multiscale Effects in Plasma Microturbulence*, Ph.D. thesis, Universtat Ulm (2009).
- ¹⁰⁰Y. Xiao, P. J. Catto, and W. Dorland, "Effects of finite poloidal gyroradius, shaping, and collisions on the zonal flow residual," *Physics of Plasmas* **14**, 055910 (2007).
- ¹⁰¹F. Romanelli and F. Zonca, "The radial structure of the ion-temperature-gradient-driven mode," *Physics of Fluids B: Plasma Physics* **5**, 4081–4089 (1993).
- ¹⁰²I. M. Benn and S. T. Shanahan, "Of lightning rods, charged conductors, curvature, and things," *American Journal of Physics* **59**, 658–660 (1991).